JOURNAL OF COMPUTATIONAL PHYSICS 26, 408–442 (1978)

Long-Time-Scale Simulation of Resonant Particle Effects in Langmuir and Whistler Waves

C. E. RATHMANN,* J. L. VOMVORIDIS, AND J. DENAVIT

Department of Mechanical Engineering and Astronautical Sciences, Technological Institute, Northwestern University, Evanston, Illinois 60201

Received February 18, 1977

The time scale of conventional particle simulation methods is limited by electron dynamics to time steps Δt which satisfy the conditions $\omega_p \Delta t \ll 1$, $\Omega \Delta t \ll 1$ and $k_{\max} v_{\max} \Delta t \ll 1$, where ω_p is the electron plasma frequency, Ω is the electron cyclotron frequency, $k_{\max}$ is the largest wavenumber and $v_{\max}$ is the maximum electron velocity considered in the computations. We present in this paper a one-dimensional particle-pushing algorithm in which particles are advanced, during each time step, along trajectories which are first-order in the field amplitudes. In this algorithm the time step is limited by the nonlinearities and inhomogeneities and must satisfy the conditions $\omega_t \Delta t \ll 1$, and $\kappa v_{\max} \Delta t \ll 1$, where ω_t ($\ll \omega_p$, Ω) is the electron trapping frequency and κ ($\ll k_{\max}$) is the inverse characteristic length of the inhomogeneities. Two versions of the algorithm, corresponding to Langmuir and whistler waves are given. This algorithm is applicable to problems in which the plasma may be considered to consist of a dense cold component and of a sparse energetic component, such as occur in plasma-beam interactions and in magnetospheric studies. Wave propagation in the cold plasma may then be represented by a fluid model, while resonant wave-particle interactions in the energetic plasma are computed using the present long-time-scale algorithm. Tests of the accuracy of the algorithm and examples of applications to Langmuir and whistler waves are presented.

INTRODUCTION

Particle simulations, in which a plasma is represented by a large number of charged particles moving in their self- and externally-applied fields, have provided an important tool in the understanding of wave phenomena involving resonant particle interactions, which cannot be represented by a fluid model. In these simulations, the particles are usually advanced assuming the fields acting on the particles to be constant during each time step, and the fields are updated after each time step in accordance with Maxwell's equations using the new positions and velocities of the particles [1–9]. For Langmuir waves (electron plasma oscillations) the time scale of this method is limited by electron dynamics which requires the time step Δt to satisfy the conditions $\omega_p \Delta t \ll 1$ and $k_{\max} v_{\max} \Delta t \ll 1$, where $k_{\max}$ is the maximum wave number considered in the computations, $v_{\max}$ is the maximum electron velocity and ω_p is the electron

* Present address: Mission Research Corporation, Santa Barbara, CA 93102.

0021-9991/78/0263-0408$02.00/0

plasma frequency. In the case of whistler waves (electron cyclotron oscillations) an additional limitation is given by $\Omega \Delta t \ll 1$, where Ω is the electron cyclotron frequency. For most applications, these conditions prohibit Δt from being larger than $\Delta t \simeq 0.2\, \omega_p^{-1}$ (or $\Delta t \simeq 0.2\, \Omega^{-1}$), so that particle simulations of phenomena varying on a time scale much slower than ω_p^{-1} (or Ω^{-1}) may become unfeasible because of computer limitations.

In many applications it is expedient to accelerate the time scale, for example by doing the simulation with a reduced ion to electron mass ratio ($m_i/m_e = 100$) or by utilizing a relatively short system. However, this acceleration of the time scale is not always possible. Examples of such cases occur in the study of plasma turbulence caused by low intensity electron beams, or in the study of very-low-frequency emissions from the magnetosphere, where energetic electrons interact with long whistler wavepackets in an inhomogeneous magnetic field [10, 11].

In this paper we present particle-pushing algorithms in which the particles, during each time step, follow trajectories which are first-order with respect to the wave fields and with respect to the inhomogeneities of either the medium or the waves. Thus, the numerical solution may be considered as a succession of linear and spatially homogeneous solutions, reinitialized after each time step to account for nonlinearities in the particle dynamics or in the wave propagation, and for inhomogeneities due to density or external field gradients. In this method, the time step is therefore limited by nonlinearities and inhomogeneities, rather than by the frequency or wavelength of the oscillations, and must satisfy the conditions $\omega_T \Delta t \ll 1$ and $\kappa v_{\max} \Delta t \ll 1$, where $\omega_T \ll \omega_p$, Ω is the electron trapping frequency and $\kappa \ll k_{\max}$ is the inverse characteristic length of the inhomogeneities.

The application of this long-time-scale algorithm requires that during each time step, the internal fields be expressed as a sum of individual waves,

$$E(x, t) = \sum_{n=1}^{n_{\max}} \mathscr{E}_n e^{i\psi_n} \tag{1}$$

where the quantities $\mathscr{E}_n(x, t)$ and $\psi_n(x, t)$ are respectively the amplitude and the phase of each wave n. The wave frequencies $\omega_n = \partial\psi_n/\partial t$ and wave numbers $k_n = -\partial\psi_n/\partial x$ as well as the amplitudes $\mathscr{E}_n$ are assumed to be slowly varying functions of time and space over the periods $2\pi/\omega_n$ and the wavelengths $2\pi/k_n$ of the oscillations.

It is possible in some applications to consider a plasma as consisting of two components, viz., a high-density cold component, which constitutes the major propagation medium and a low-density energetic electron component, which is responsible for resonant particle interactions. In such cases, wave propagation in the plasma may be formulated using a fluid model of the cold electron component, giving equations of propagation for the amplitudes and phases of the form

$$\mathscr{F}_n(\mathscr{E}_n) = \mathscr{S}_n(x, t), \tag{2}$$

$$\mathscr{G}_n(\psi_n) = \mathscr{C}_n(x, t), \tag{3}$$

where $\mathscr{F}_n$ and $\mathscr{G}_n$ are differential operators with respect to space and time, which account for the propagation in the cold component, while $\mathscr{C}_n$ and $\mathscr{S}_n$ are source terms due to the charge and current densities of resonant energetic particles. For problems in which the plasma can be separated into cold and energetic components in this manner, hybrid (fluid-and-particle) simulations may be done as illustrated symbolically in Fig. 1. The internal fields are represented as a sum of waves according to Eq. (1), and Eqs. (2) and (3), describing wave propagation in the cold plasma, are used to advance the field amplitudes and phases, $\mathscr{E}_n$ and ψ_n, over a time step Δt. The energetic electrons are then advanced over the time step according to their first-order orbits in the wave fields, and the new positions and velocities of these particles are used to update the source terms $\mathscr{S}_n$ and $\mathscr{C}_n$ to be used to advance the field amplitudes over the following time step.

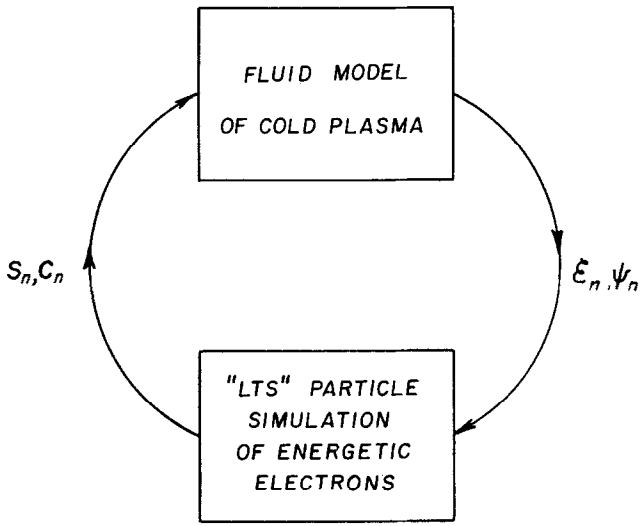

FIG. 1. Symbolic diagram of a hybrid fluid-particle code using the long time scale (LTS) particle-pushing algorithm.

Two versions of the algorithm, applicable to Langmuir waves (electron plasma oscillations) and to whistler waves (electron cyclotron oscillations) are presented respectively in Parts I and II of the paper.

I. LANGMUIR WAVES

The velocity and position increments for electrons in a longitudinal electric field corresponding to one-dimensional Langmuir waves are derived in Section I.1, and test-particle trajectories in single-mode and two-mode electric fields are presented in Section I.2. In the present case for which the phase space is limited to two dimensions,

the electron distribution is represented on an (x, v) grid and is reconstructed at each time step [6]. This application of the algorithm to a Vlasov solution is given in Section I.3 and allows the introduction of weak collisional effects on resonant particles [7]. The equations governing the evolution of the electric field are derived in Section I.4 and several examples of application are given in Section I.5.

I.1. Velocity and Position Increments

We consider in this section the motions of electrons in a one-dimensional electric field represented in terms of the Fourier series

$$E(x, t) = \sum_{n=1}^{N} \mathscr{E}_n(t) \sin[k_n x + \alpha_n(t)], \tag{4}$$

where $k_n = 2\pi n/L$ denotes fixed wave numbers and L is the length of the system. Periodic boundaries are assumed here, although this condition will be relaxed in Part II when dealing with cyclotron waves. The mode amplitudes $\mathscr{E}_n(t)$ and frequencies $\omega_n(t) = -\dot{\alpha}_n$ are assumed to very slowly relative to the frqeuencies ω_n, i.e., $\dot{\mathscr{E}}_n/\omega_n \mathscr{E}_n \ll 1$ (dots denote time differentiation).

The velocity v_i and position x_i of a particle i are advanced during the time interval from t to $t + \Delta t$ according to the first-order motion of the particle with respect to the electric field [12, 13]. The velocity and position increments may therefore be expressed as sums of increments due to each wave,

$$v_i(t + \Delta t) = v_i(t) + \sum_n \delta v_{in} + O(E^2), \tag{5}$$

$$x_i(t + \Delta t) = x_i(t) + v_i(t)\,\Delta t + \sum_n \delta x_{in} + O(E^2), \tag{6}$$

where δv_{in} and δx_{in} denote the velocity and position increment of particle i due to its interaction with wave n.

To first order in E, the velocity of a particle i, interacting with a single wave n is given by

$$\begin{aligned} v_i(t') &= v_i(t) - \frac{e}{m} \int_t^{t'} \mathscr{E}_n \sin\{k_n[x_i(t) + (t'' - t)\, v_i(t)] + \alpha_n(t) \\ &\quad - (t'' - t)\, \omega_n(t)\}\, dt'' + O(\mathscr{E}_n{}^2), \\ &= v_i(t) + \frac{e\mathscr{E}_n}{mR_{in}} \{\cos[\psi_{in} + k_n(t' - t)\, u_{in}] - \cos \psi_{in}\} + O(\mathscr{E}_n{}^2), \end{aligned} \tag{7}$$

where $-e$ and m are the electron charge and mass respectively, $u_{in} = v_i - \omega_n/k_n$ denotes the velocity of particle i relative to the phase velocity of the wave, $\psi_{in} = \alpha_n + k_n x_i(t)$ is the initial particle phase and $R_{in} = k_n u_{in}$. Here the slowly varying

functions $\mathscr{E}_n$ and ω_n have been held constant during the time step Δt. A similar integration yields

$$x_i(t') = x_i(t) + v_i(t)(t' - t) + \frac{e\mathscr{E}_n}{mR_{in}^2}\{\sin[\psi_{in} + k_n(t' - t)\,u_{in}] - \sin\psi_{in} - R_{in}(t' - t)\cos\psi_{in}\} + O(\mathscr{E}_n^2). \tag{8}$$

Setting $t' = t + \Delta t$ and rearranging terms gives the first-order velocity and position increments during a time step,

$$\delta v_{in} = \frac{e\mathscr{E}_n}{m}\Delta t\left[\cos\psi_{in}\left(\frac{\cos\theta_{in} - 1}{\theta_{in}}\right) - \sin\psi_{in}\left(\frac{\sin\theta_{in}}{\theta_{in}}\right)\right], \tag{9}$$

$$\delta x_{in} = \frac{e\mathscr{E}_n}{m}\Delta t^2\left[\cos\psi_{in}\left(\frac{\sin\theta_{in} - \theta_{in}}{\theta_{in}^2}\right) + \sin\psi_{in}\left(\frac{\cos\theta_{in} - 1}{\theta_{in}^2}\right)\right], \tag{10}$$

where $\theta_{in} = k_n(v_i - \omega_n/k_n)\,\Delta t$ is a resonance parameter. Substitution of Eqs. (9) and (10) into Eqs. (6) and (5) provides the algorithm for advancing particles over a time step [14].

By introducing the trapping frequency $\omega_{Tn} = (e\mathscr{E}_n k_n/m)^{1/2}$ and the trapping velocity $v_{Tn} = 2\omega_{Tn}/k_n$ of a particle in the potential well of wave n, Eqs. (9) and (10) may be recast in the form $\delta v_{in}/v_{Tn} = \frac{1}{2}(\omega_{Tn}\,\Delta t)\,V_{in}$ and $k_n\,\delta x_{in} = (\omega_{Tn}\,\Delta t)^2\,X_{in}$ where V_{in} and X_{in} denote the square brackets in Eqs. (9) and (10) respectively. Thus the velocity and position increments appear as the first terms of expansions in powers of $\omega_{Tn}\,\Delta t$, suggesting that the time step in the present algorithm is limited by the conditions $\omega_{Tn}\,\Delta t \ll 1$. This may be verified by considering the variation δH_{in} of the Hamiltonian $H_{in} = -e\mathscr{E}_n(\cos\psi_{in} + 1)/k_n + \frac{1}{2}mu_{in}^2$ of a particle i in the potential well of a wave n. This quantity is an invariant for infinitesimal time intervals and its variation for finite Δt satisfies the condition $\delta H_{in}/H_{n0} \lesssim (\omega_T\,\Delta t)^2$ where $H_{n0} = \frac{1}{2}mv_{Tn}^2$ is the depth of the potential well. The numerical tests presented in the next Section show that this error estimate is rather conservative and that time steps $\Delta t = 0.2\,\omega_{Tn}^{-1}$ yield accurate results. In addition, Δt must satisfy the condition $\Delta t \ll T$, where $T \sim (\dot{\mathscr{E}}_n/\mathscr{E}_n)^{-1} \sim (\dot{\omega}_n/\omega_n)^{-1}$ is the characteristic time of the electric field spectrum.

I.2. Test Particle Trajectories

The accuracy of the particle-pushing algorithm is examined by computing test-particle trajectories in single-mode and two-mode electric fields.

Single-mode field: The results of these computations are shown in Fig. 2 for two different time increments $\Delta t = 0.125\,\omega_T^{-1}$ and $\Delta t = 0.625\,\omega_T^{-1}$, the errors in the algorithm being reflected in the discrepancy between the results using these two time increments. Note that particles with relative velocities $u = v - \omega/k$ less than the trapping velocity exhibit trapped motion having closed orbits in the $x - u$ plane

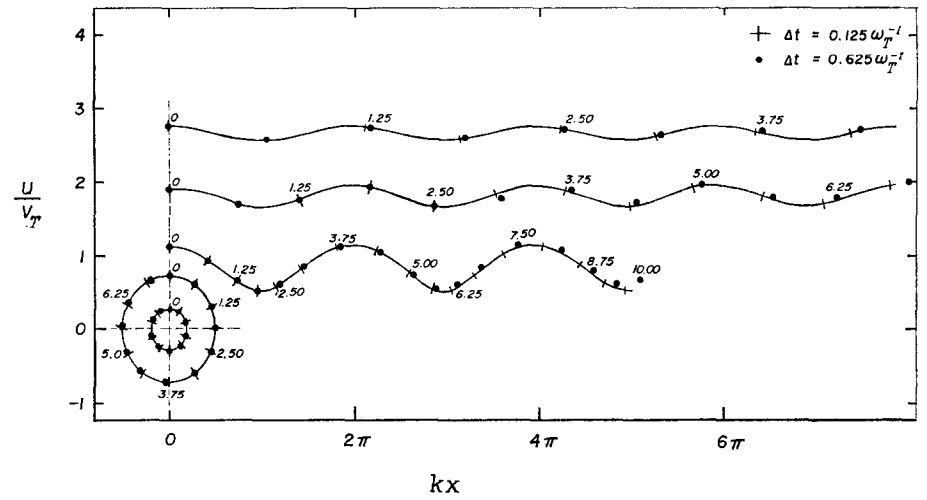

FIG. 2. Test particle trajectories in a single-mode longitudinal electric field. The reference frame is moving with the phase velocity ω/k.

of Fig. 2. The particle located near the origin $x = u = 0$, whose velocity differs only slightly from the phase velocity, has a period $\tau = \tau_T = 2\pi(eE_k/m_e)^{-1/2}$ exhibiting simple harmonic motion as it oscillates in a potential well. The trapped particle with a higher velocity has a somewhat longer period $\tau \simeq 1.2\tau_T$, also in agreement with the theory of oscillation in a sinusoidal potential well. Untrapped particles exhibit deviations from their free-streaming trajectories which decrease with increasing velocity, and even for the particle having the largest relative velocity $u = 2.8v_T$, the long time steps chosen for the simulation permit these deviations to be followed closely.

The largest discrepancies occur for the particle having an initial relative velocity just above the trapping velocity v_T. For a constant field, the trajectories in the region close to the limit cycle are very sensitive to small differences in initial conditions since such differences may mean the difference between a closed (i.e., trapped) orbit and an open (i.e., untrapped) orbit. Such errors, however, are not expected to be a serious handicap to the algorithm since in most applications the trapping velocity is expected to change continuously in time instead of being constant as in the present case.

Two-mode field: A test particle trajectory from a computation in which the electric field consists of two modes, $E(x, t) = \mathscr{E}_1 \sin(k_1x - \omega_1t) + \mathscr{E}_2 \sin(k_2x - \omega_2t)$, is shown in Fig. 3. Here the two modes have equal amplitudes, $\mathscr{E}_1 = \mathscr{E}_2 = \mathscr{E}$, and slightly different frequencies, $\omega_2/\omega_1 = 1.095$, and wave numbers, $k_2/k_1 = 1.1$. These values give phase velocities $v_{p1} = \omega_1/k_1$ and $v_{p2} = \omega_2/k_2$, with $v_{p2}/v_{p1} = 0.9954$. This field may be written in the form $E(x, t) = 2\mathscr{E} \sin\{\frac{1}{2}[(k_1 + k_2)x - (\omega_1 + \omega_2)t]\}$ $\cos\{\frac{1}{2}[(k_1 - k_2)x - (\omega_1 - \omega_2)t]\}$ showing that the potential is sinusoidal and travels at the phase velocity $v_p = (\omega_1 + \omega_2)/(k_1 + k_2) = 1.00217v_{p2}$ within a sinusoidal

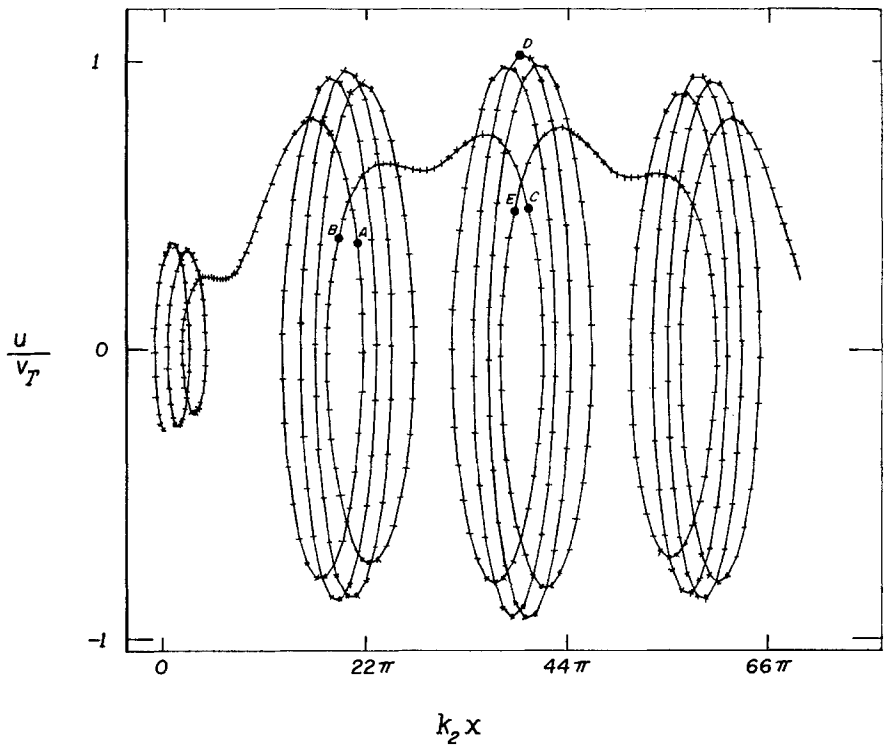

FIG. 3. Test particle trajectory in a two-mode longitudinal electric field with $\mathscr{E}_1 = \mathscr{E}_2$, $k_2/k_1 = 1.1$ and $\omega_2/\omega_1 = 1.095$. The reference frame is moving with the phase velocity of the slower wave, ω_2/k_2. The particle undergoes trapping oscillations from A to B, becomes untrapped as the potential well approaches a node, moving from B to C, after which it undergoes another series of trapping oscillations from C to E. The time step is $\Delta t = \tau_T/30$.

envelope which moves at the group velocity $v_g = (\omega_1 - \omega_2)/(k_1 - k_2) = 0.95434 v_{p2}$. The reference frame of Fig. 3 moves at the phase velocity v_{p2} of the slower wave, giving relative phase and group velocities $v_p' = v_p - v_{p2} = 0.00217 v_{p2}$ and $v_g' = v_g - v_{p2} = -0.04566 v_{p2}$. The trapping frequency of the second mode is $\omega_{T2} = (e\mathscr{E}k_2/m_e)^{1/2} = 0.0205\omega_2$ and the potential well travels from one node to the next in a time $T = 29.58\omega_{T2}^{-1}$.

The trajectory shown in Fig. 3 is interpreted as follows: A test particle initially trapped within a potential well oscillates and moves with it as shown by the almost closed orbits from A to B. As the node of the potential envelope is encountered, the potential well disappears and the particle free-streams from B to C until it encounters a deepening potential well on the other side of the node. As the potential well deepens further, the particle undergoes another set of trapping oscillations from C to E, reaching a maximum velocity at D. When another node is approached the potential well again becomes shallow, the maximum velocity decreases until the potential well disappears, the particle free-streams again, and the process is repeated.

This computation was carried out with $\Delta t = \tau_T/30$ and with $\Delta t = \tau_T/6$. Both intervals gave accurate results over 15 trapping periods and show that the algorithm accounts correctly for transitions between trapped and untrapped motions when the potential well amplitude varies in time.

I.3. Evolution of the Distribution Function

In the present algorithm which corresponds to a two-dimensional phase space, the distribution function is conveniently represented on a grid covering the region of the (x, v) plane which includes resonant particles, as shown in Fig. 4. Here $v_{\max}$ and $v_{\min}$ denote the maximum and minimum velocities, v_k with $k = 1,..., K$, denotes the grid point velocities and $x_j = j\,\Delta x$ denotes the grid point positions, where $j = 1,..., J$, $\Delta x = L/J$, and L is the length of the system. Particles whose weights are proportional to the local values of the distribution function are initialized at the grid points and advanced from them by increments δx_{jk} and δv_{jk} according to Eqs. (5), (6), (9), (10), where the subscript pair (j, k) now designates the particle. After a time step Δt, each particle is redistributed among its neighboring grid points by a local smoothing operation in phase space [6, 7]. In this manner the distribution function is reconstructed and the particles are re-initialized at the grid points prior to the application of the following time step.

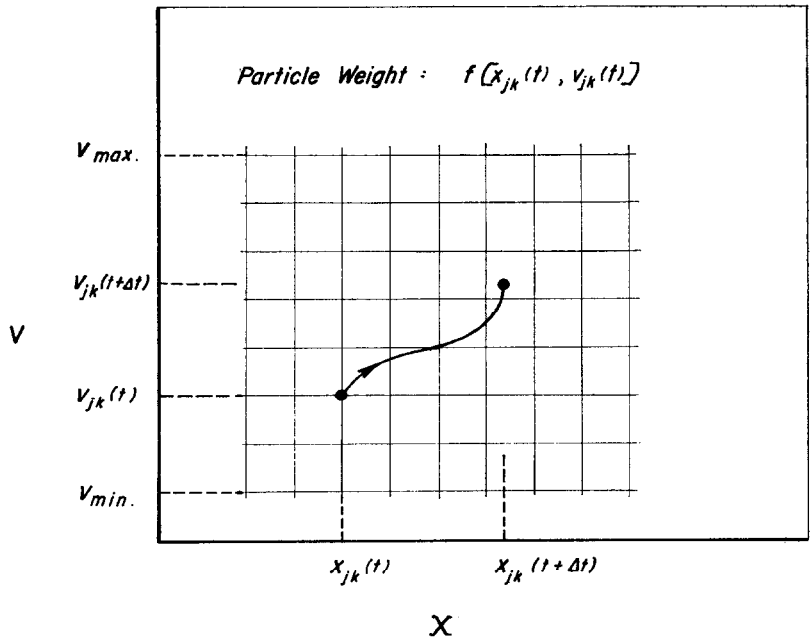

Fig. 4. Phase plane representation of the distribution function $f(x, v)$ for Langmuir waves in terms of weighted particles distributed in a rectangular grid (x_{jk}, v_{jk}). The curved line, representing a particle's trajectory during one time step, may cover several grid spacings.

Note that because of the regular arrangement of particles on the (x, v) grid at the beginning of each time step, the initial phases $\psi_{jn} = 2\pi jn/J + \alpha_n(t)$ apply to all particles at position $j\Delta x$, regardless of their velocities. Hence, the trigonometric functions $\sin \psi_{jn}$ and $\cos \psi_{jn}$ do not need to be evaluated for each particle but only at each grid point position $j\Delta x$. Similarly the resonance parameters $\theta_{kn} = 2\pi n(v_k - \omega_n/k_n)\Delta t/L$ need to be evaluated only at the velocity grid points v_k.

Collisional effects are included in the algorithm in terms of the one-dimensional Fokker-Planck operator

$$\left(\frac{\partial f}{\partial t}\right)_{\text{coll}} = \frac{\partial}{\partial v}\left[\nu v f + D\frac{\partial}{\partial v}(\nu f)\right], \tag{11}$$

where $\nu(v)$ is a velocity-dependent collision frequency and D is a parameter which may be specified to give energy conservation by setting $D = \int v^2 \nu f\, dv / \int \nu f\, dv$ [7]. The collisional operator (11) includes both a frictional effect represented by the first term in the bracket, and a velocity diffusion effect represented by the second term.

For weak collisions satisfying the stability condition $2D\Delta t \nu_k/(\Delta v_{k-1}\Delta v_k) \leqslant 1$, where $\Delta v_k = v_{k+1} - v_k$, the diffusion term may be represented by an explicit finite difference procedure. If z_k denotes the particle weight at the velocity grid point k, its increment due to diffusion is given by

$$\delta z_k = 2D\,\Delta t\left\{\frac{(\nu z)_{k+1}}{\Delta v_k(\Delta v_k + \Delta v_{k+1})} - \frac{(\nu z)_k}{\Delta v_{k-1}\,\Delta v_k} + \frac{(\nu z)_{k-1}}{\Delta v_{k-1}(\Delta v_{k-1} + \Delta v_{k-2})}\right\}, \tag{12}$$

in which a non-uniform velocity grid spacing has been assumed. For collision frequencies which do not satisfy the stability condition, Eq. (12) is applied as a sequence of l steps, each with a coefficient $2D\Delta t/l$ sufficiently small to satisfy the stability condition.

The collisional friction term is implemented by restarting the particles after each time step with velocities $\bar{v}_k = (1 - \nu_k\,\Delta t)v_k$. In this case the resonance parameters become $\theta_{nk} = 2\pi n(\bar{v}_k - \omega_n/k_n)\Delta t/L$ but the computation of the position and velocity increments is otherwise unchanged.

I.4. Evolution of the Electric Field

The electric field $E(x, t)$ is associated with a Langmuir wave propagating in a plasma consisting of a dense low-energy component and of a sparse energetic component. In the simplest model considered here the ions are stationary and the low-energy electrons are described by linearized continuity and momentum equations, neglecting thermal motion. More complete *fluid* models of the low-energy component, including pressure forces, ion motions and nonlinearities, may be introduced, but resonant particles must be confined to the energetic component of the plasma which is described in terms of its distribution function using the algorithm discussed in Section I.1.

From Poisson's equation, $\partial E/\partial x = -4\pi e(\tilde{n}_p + \tilde{n}_E)$, where $\tilde{n}_p$ and $\tilde{n}_E$ denote respectively the cold and energetic electron density perturbations. Differentiating this equation twice with respect to time and substituting the expressions for $\tilde{n}_p$ and $\tilde{n}_E$ obtained from the cold electron equations and from the equation of continuity for the energetic electrons yields

$$\frac{\partial}{\partial x}\left\{\frac{\partial^2 E}{\partial t^2} + \omega_p{}^2 E + 4\pi \frac{\partial J_E}{\partial t}\right\} = 0, \tag{13}$$

where $\omega_p{}^2 = 4\pi e^2 n_p/m$ is the electron plasma frequency for the cold component and J_E is the energetic electron current density.

After Fourier transformation with respect to the space coordinate, Eq. (13) takes the form

$$\frac{d^2}{dt^2}[\mathscr{E}_n \exp(i\alpha_n)] + \omega_p{}^2 \mathscr{E}_n \exp(i\alpha_n) = -\frac{8\pi i}{L}\frac{d}{dt}\int_0^L J_E e^{-ik_n x}\, dx,$$

where $J_E = -e\sum_i v_i \delta(x - x_i)$, in which the sum is taken over energetic particles with position x_i and velocity v_i located in a cylinder of unit cross-section perpendicular to x. Setting $\omega_n = -\dot{\alpha}_n$ as the frequency of mode n, and separating real and imaginary parts gives

$$\ddot{\mathscr{E}}_n - (\omega_n{}^2 - \omega_p{}^2)\mathscr{E}_n = \dot{S}_n + \omega_n C_n, \tag{14}$$

$$2\omega_n \dot{\mathscr{E}}_n + \dot{\omega}_n \mathscr{E}_n = -\dot{C}_n + \omega_n S_n, \tag{15}$$

where

$$C_n = \frac{8\pi e}{L}\sum_i v_i \cos(k_n x_i + \alpha_n), \tag{16}$$

and

$$S_n = \frac{8\pi e}{L}\sum_i v_i \sin(k_n x_i + \alpha_n) \tag{17}$$

depend on the correlation of energetic particles relative to mdoe n. The correlation terms C_n and S_n vary slowly compared to the high frequencies ω_n, so that we may neglect $\dot{S}_n \ll \omega_n C_n$ and $\dot{C}_n \ll \omega_n S_n$ in Eqs. (14) and (15). Writing $\omega_n = \omega_p + \tilde{\omega}_n$, assuming a small frequency shift, $\tilde{\omega}_n \ll \omega_p$ and neglecting the second order derivative $\ddot{\mathscr{E}}_n \sim \tilde{\omega}^2 \mathscr{E}_n$ yields

$$\tilde{\omega}_n = -\frac{C_n}{2\mathscr{E}_n}. \tag{18}$$

After multiplication by $\mathscr{E}_n$ the left member of Eq. (15) becomes $d(\omega_n \mathscr{E}_n{}^2)/dt$. Introducing the wave energy density of mode n (sum of the cold plasma potential and

kinetic energy densities for this mode) $U_n = (\omega_p^2/\omega_n^2 + 1)\mathscr{E}_n^2/8\pi$ and integrating over the interval Δt yields

$$\delta U_n = \frac{\mathscr{E}_n}{8\pi} S_n \Delta t. \tag{19}$$

The quantities C_n and S_n therefore appear as source terms representing contributions of energetic particles to the frequency and energy of each wave. Updated values of these quantities are computed at each time step from the positions and velocities of the energetic electrons.

I.5. Examples of Long-Time-Scale Simulations

We present in this Section applications of the algorithm (i) to the instability and trapping of a low-density energetic beam, (ii) to large-amplitude Langmuir oscillations and (iii) to the instability of a diffuse beam. Simulations which consider weak collisional effects on resonant particle interactions are included.

(i) *Instability and Trapping of a Monoenergetic Beam*

We consider unstable Langmuir oscillations excited in a cold plasma of density n_p by a low-density monoenergetic beam of velocity v_d and density $n_b \ll n_p$. The maximum growth rate of this instability is $\gamma_{\max} = (\sqrt{3}/2)\,\omega_p(n_b/2n_p)^{1/3}$ and occurs for the wave number $k \simeq \omega_p/v_d$. The frequency shift of this unstable mode is $\tilde{\omega} = -(n_b/2n_p)^{1/3}\omega_p/2$. The wave amplitude $\mathscr{E}$ grows exponentially until the trapping frequency $\omega_T = (e\mathscr{E}k/m)^{1/2}$ reaches a value comparable to the grwoth rate $\gamma_{\max}$, at which time trapping oscillations of the resonant particles prevent further growth and cause the amplitude to oscillate at approximately the trapping frequency.

To simulate this instability, the amplitude $\mathscr{E}$ and frequency ω of a monochromatic Langmuir wave propagating in the cold plasma are followed in time by Eqs. (18) and (19). The beam particles are advanced in time using the algorithms of Sections I.1 and I.3, providing values of the source terms C_n and S_n used at each time step in Eqs. (18) and (19) to update the wave amplitude and frequency.

The results of a simulation with a beam having an initial distribution $f_b = n_b \exp[-(v - v_d)^2/2v_b^2]/2\pi$, with $n_b/n_p = 3 \times 10^{-6}$, $v_b = 1.25 \times 10^{-3}v_d$ and $\omega_p/k = 0.9977v_d$ are given in Fig. 5. This simulation was done with a system of length $L = 2\pi/k$ divided into 32 intervals Δx and with time increments $\Delta t = 12.5\omega_p^{-1}$ and $25\omega_p^{-1}$. A uniform grid with $\Delta v = 0.16v_B$ was used with a two-point reconstruction scheme using linear weight functions [6]. Only a strip of phase space with $|v - v_d| \leqslant 100v_b$ need be considered here.

The wave amplitude $\mathscr{E}$, plotted in Fig. 5a, is observed to exponentiate over two orders of magnitude at a rate $\gamma = 8.85 \times 10^{-3}\omega_p$ which is in agreement with the theoretical value $\gamma_{\max} = 9.91 \times 10^{-3}\omega_p$. Saturation occurs when the amplitude reaches a level for which the saturation trapping frequency $\omega_{Ts} = 0.0137\omega_p$ is

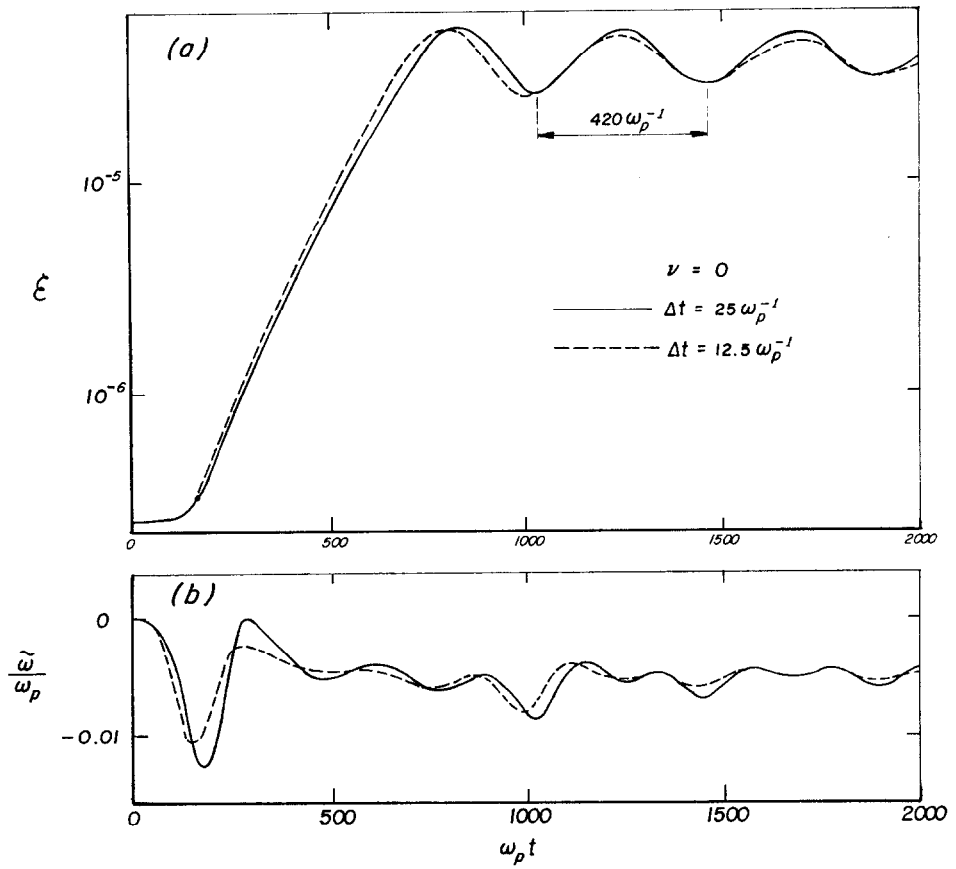

FIG. 5. Electric field amplitude $\mathcal{E}$ and frequency shift $\tilde{\omega}$ for a Langmuir instability resulting from the interaction of a monoenergetic electron beam with a cold plasma. The amplitude is measured in units of $mL\omega_p^2/e$.

approximately equal to the growth rate γ, and after saturation the amplitude oscillates near the trapping frequency as expected. The frequency shift $\tilde{\omega} = \omega - \omega_p$, given in Fig. 5b, reaches an approximately constant value $\tilde{\omega} \sim 5 \times 10^{-3}\omega_p$, close to the theoretical value $5.7 \times 10^{-3}\omega_p$, during the growth period, after which it is observed to oscillate near the trapping frequency. No significant differences are observed in Fig. 5 between the results using $\Delta t = 12.5\omega_p^{-1}$ ($\omega_{Ts}\,\Delta t = 0.17$) and $\Delta t = 25\omega_p^{-1}$ ($\omega_{Ts}\,\Delta t = 0.34$). Trapping of the beam particles is clearly seen in the phase space plots of Fig. 6 where the development of the trapping vortex and the subsequent mixing in phase is evident.

The results of two additional simulations including weak collisions with collision frequencies $\nu = 2 \times 10^{-8}\omega_p$ and $\nu = 4 \times 10^{-8}\omega_p$ are compared in Fig. 7 with the collisionless case. Note that such small collision frequencies do not have a large effect

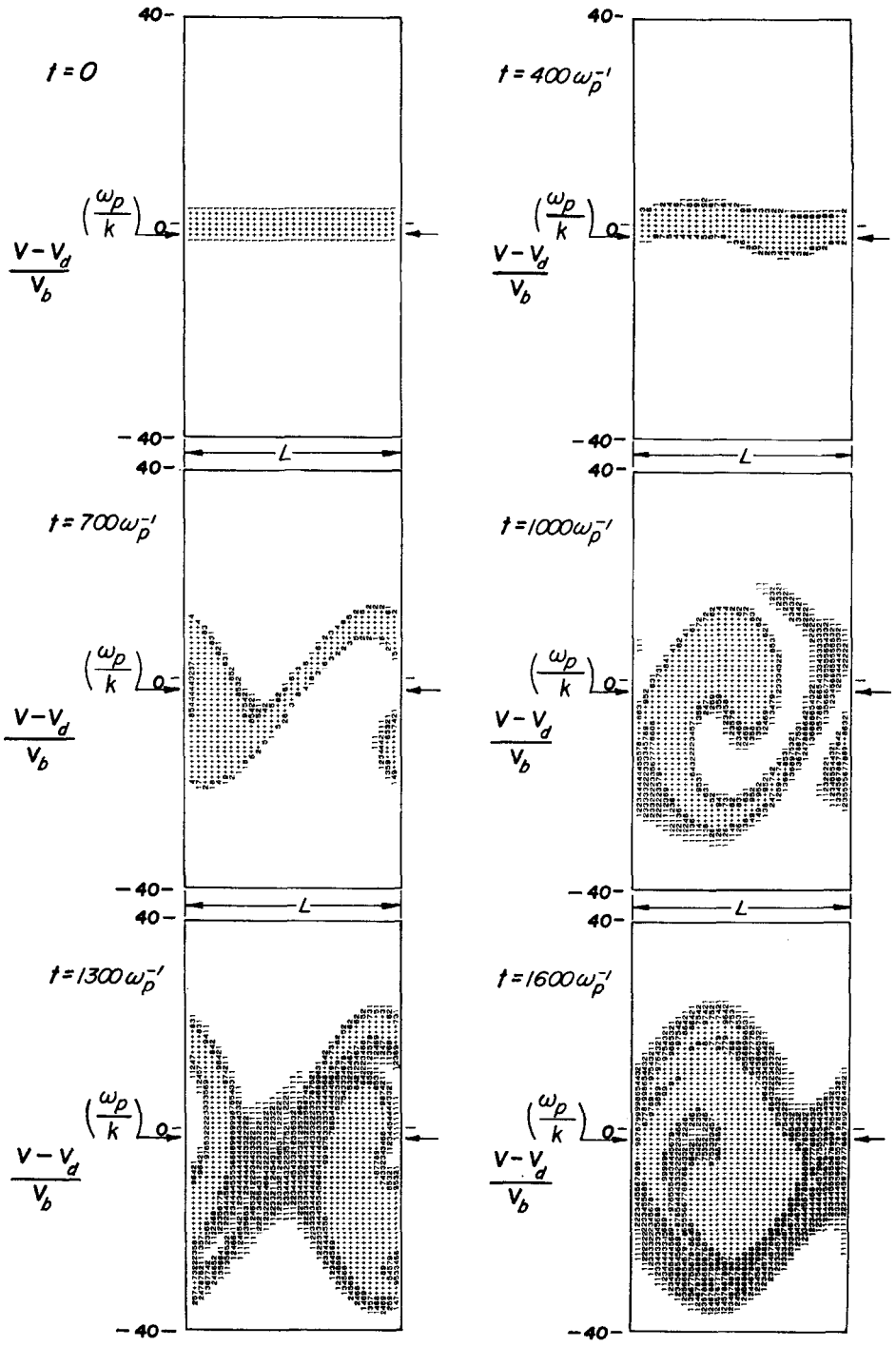

FIG. 6. Phase space plots showing the instability and trapping the monoenergetic electron beam corresponding to Fig. 5.

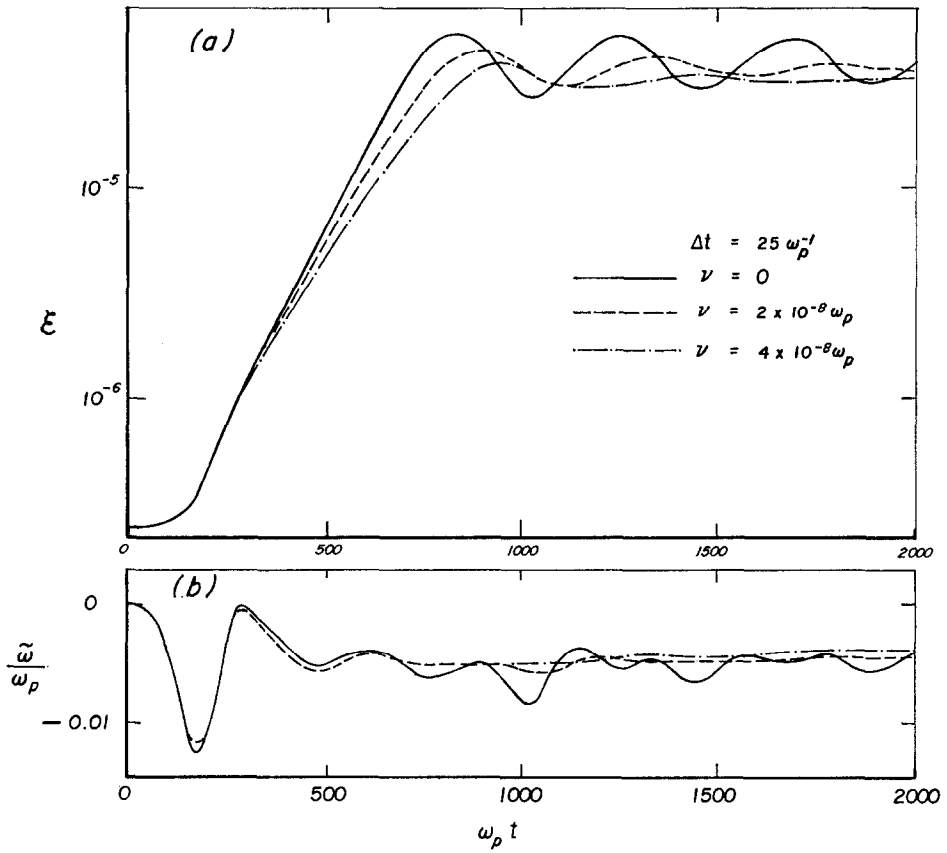

FIG. 7. Effect of weak collisions on the Langmuir instability and trapping of a monoenergetic electron beam.

on the growth rate of the instability or on the frequency shift during the growth period but damp the trapping oscillations rapidly.

(ii) *Large-Amplitude Langmuir Oscillations*

For large-amplitude Langmuir oscillations characterized by a trapping frequency ω_T approximately equal to the Landau damping rate γ_L, the electrons trapped in the potential well of a stable Langmuir wave modify the distribution function in the resonant region. In this case, Landau damping takes place only during an initial period, after which the wave amplitude is modulated at approximately the trapping frequency [15–17].

To simulate this phenomenon, the amplitude and frequency of the Langmuir wave are again followed in time using the formalism of Section I.4. Resonant energetic electrons, which contribute to the source terms C_n and S_n, are followed in time by the algorithm of Sections I.1 and I.3. These particles are given an initial Maxwellian

distribution $f_E = n_E \exp(-v^2/2v_{th}^2)/(2\pi)^{1/2} v_{th}$, with $n_E/n_0 = 1.7 \times 10^{-3}$. The wave is initialized with an amplitude corresponding to the trapping frequency $\omega_T = 5 \times 10^{-3}\omega_p$ and a wave number $k = \omega_p/v_{th}$ corresponding to a phase velocity near the thermal velocity of the energetic electrons.

In the present case, only a narrow band of phase plane needs to be considered, with $v_{\min} = v_{th} - u_c$ and $v_{\max} = v_{th} + u_c$. Values of u_c equal to $5v_T$ and $10v_T$, where $v_T = 2\omega_T/k$ denotes the initial trapping velocity, have been considered with a velocity interval $\Delta v = v_T/12$. Boundary conditions are imposed to maintain continuous values of $f(x, v)$ and $\partial f/\partial v$ near $v_{\min}$ and $v_{\max}$ after each reconstruction of the distribution function. Let δv_b denote the maximum velocity increment of a particle at the boundaries during a time step. For a two-point reconstruction scheme, at most $|\delta v_b|/\Delta v + 1$ velocity grid points near each boundary ($v_{\max}$ or $v_{\min}$) are affected by the absence of simulation particles outside the boundaries. For a four-point reconstruction scheme,

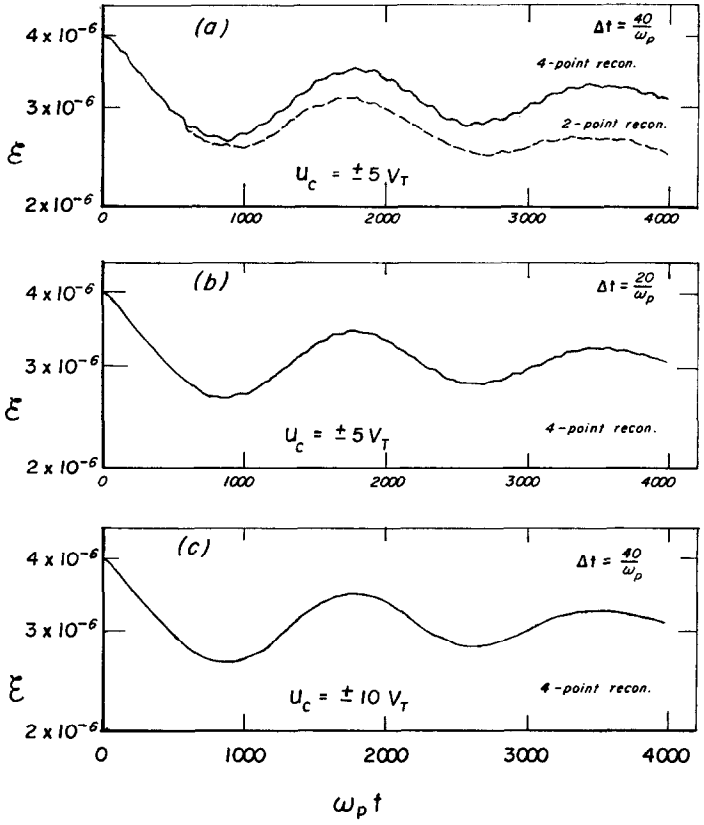

FIG. 8. Electric field $\mathscr{E}$ for large amplitude Langmuir oscillations. The amplitude modulation with period $\simeq 125\ \omega_p^{-1}$, observed in (a) for the four-point reconstruction scheme, is a boundary effect associated with the finite velocity interval considered here. It is significantly reduced by either reducing the time step as shown in (b) or by increasing the width of the velocity interval as shown at (c). The field amplitude is measured in units of $mL\omega_p^2/e$.

at most $|\delta v_b|/\Delta v + 2$ points are affected. Values of f at these boundary points are extrapolated from the adjacent interior points to maintain values of $\partial^2 f/\partial v^2 = -(1 - v^2/v_{th}^2) f/v_{th}^2$, corresponding to a local Maxwellian distribution function near the boundaries. The periodicity length of the system, equal to the wavelength, $L = 2\pi/k$, is divided into 32 intervals Δx.

The results of a series of simulations for the collisionless case are given in Fig. 8. We observe in Fig. 8a a significant difference between the results obtained using the two-point and the four-point reconstruction schemes. As in conventional numerical solutions of the Vlasov equation the present method is subject to numerical diffusion which is particularly evident in the present case since, like collisions, it allows electrons to escape from the potential trap of the wave. All further simulations in the present case have been done using the "energy conserving" four-point reconstruction scheme [6]. The results shown in Figs. 8b and 8c correspond respectively to a smaller time step and to a wider band of simulation particles. These simulations agree closely in their general features with the four-point simulation of Fig. 8a. After an initial decay which is in close agreement with Landau damping, $\gamma_L = 0.65 \times 10^{-3}\omega_p$ the amplitude is modulated at approximately the trapping frequency, $\omega_{Tav} = 4.47 \times 10^{-3}\omega_p$ corresponding to the mean amplitude $\langle \mathscr{E} \rangle = 0.8\mathscr{E}(t = 0)$. This modulation is observed to decay but the mean value of the amplitude remains approximately constant as trapped particles phase mix after several trapping oscillations.

In addition to these general features, the simulations of Fig. 8 also show a high-frequency amplitude modulation. In the four-point reconstruction result of Fig. 8a this modulation is particularly evident and has a period $125\omega_p^{-1}$ which corresponds precisely to the transit time of a boundary particle across the wavelength in the wave frame, $\tau_c = 2\pi/ku_c$. This amplitude modulation is the result of an inaccurate representation of the distribution function at the boundary points and is significantly reduced when δv_b is reduced, either by reducing Δt, as in Fig. 8b, or by increasing the half width u_c of the band of simulation particles, as in Fig. 8c.

Another series of simulations was carried out to study the effect of collisions on trapping oscillations. The results of these computations, given in Fig. 9, show that even very weak collisions, with collision frequencies ranging from $\nu = 0.4 \times 10^{-8}\omega_p$ to $4 \times 10^{-8}\omega_p$ are effective in allowing trapped particles to escape from the potential well of the wave. For $\nu = 4 \times 10^{-8}\omega_p$, no significant trapping remains and the field decays at a rate close to the Landau damping rate for $t > 2000\omega_p^{-1}$. These conclusions are in agreement with previous analytical and computer simulation results [18, 19].

(iii) *Bump-on-tail Instability*

We consider now a problem involving several stable and unstable modes resulting from a diffuse electron beam moving with a drift velocity v_d relative to a stationary hot plasma. The distribution function in the resoannce region $v_{\min} \leqslant v \leqslant v_{\max}$ is given by

$$f(v) = \epsilon \left\{ f_d + f_d' \left(\frac{v - v_d}{v_b} \right) + \exp\left[-\frac{1}{2} \left(\frac{v - v_d}{v_b} \right)^2 \right] \right\}.$$

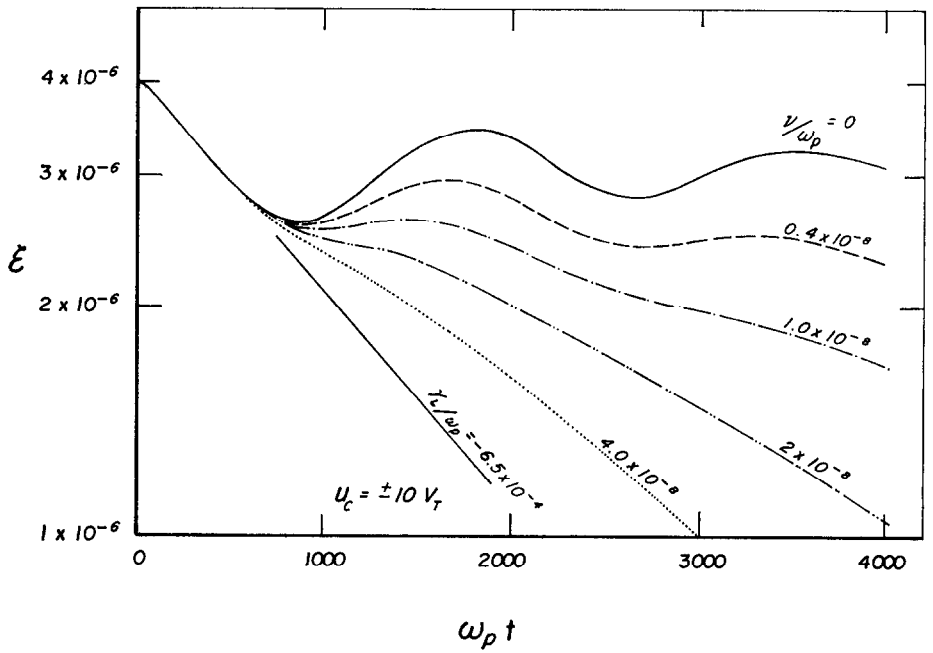

FIG. 9. Collisional effects on large-amplitude Langmuir collisions corresponding to the parameters of Fig. 8c. Note that weak collisions with $\nu \ll \gamma_L$ are effective in allowing trapped electrons to escape from the potential well of the wave.

TABLE I

Phase Velocities $(v_n - v_d)/v_b$ (Relative to Beam Velocity), Trapping Frequencies ω_{Tn}/ω_p, and Growth Rates γ_n/ω_p for Modes $n = 8,\ldots, 12$ for Bump-in-Tail Instability

			γ_n/ω_p	
n	$(v_n - v_d)/v_b$	ω_{Tn}/ω_p	Theory	Computation
8	−0.6016	0.895×10^{-3}	9.9×10^{-3}	8.7×10^{-3}
9	−1.2332	0.949×10^{-3}	10.4×10^{-3}	9.4×10^{-3}
10	−1.7384	1.000×10^{-3}	2.9×10^{-3}	2.9×10^{-3}
11	−2.5118	1.049×10^{-3}	-1.6×10^{-3}	-1.8×10^{-3}
12	−2.4963	1.095×10^{-3}	-3.3×10^{-3}	-2.5×10^{-3}

Here the first two terms in the bracket represent the distribution function of the stationary plasma, assumed to have the value ϵf_d at v_d and to vary linearly with slope $\epsilon f_d'$. The exponential term represents the beam with drift velocity v_d and thermal spread v_b. In the present computation, $\epsilon = 5.5 \times 10^{-3} v_d^{-1}$, $f_d = 0.4$ $f_d' = -0.28$, $v_b = 0.16 v_d$ and a system of periodicity length $L = 45.45 v_d/\omega_d$ is considered. Five

modes with wave numbers $k_n = 2\pi n/L$, where $n = 8,\ldots, 12$ are initially excited with equal amplitudes $\mathscr{E}_n$. The distribution function is shown in Fig. 10 and the phase velocities v_n, trapping frequencies ω_{Tn} and Landau excitation (or damping) rates γ_n are given in Table I. The theoretical rates γ_n in Table I have been computed from the approximate formula $\gamma_n/\omega_p = (\pi/2)\, v_n^2(\partial f/\partial v)\,|_{v_n}$. A band of simulation particles with $v_{\min} = v_d - 4v_b$, $v_{\max} = v_d + v_b$ and $\Delta v = v_b/24$ is used in the present case, covering the resonance regions of the 5 modes.

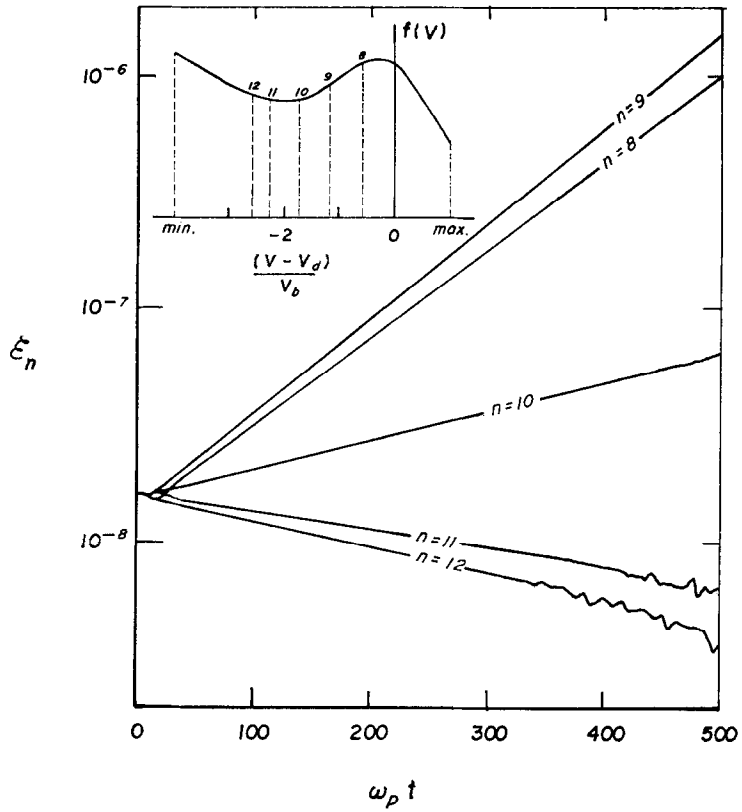

FIG. 10. Distribution function $f(v)$, in resonance region, and time development of the amplitudes $\mathscr{E}_n$ for bump-on-tail instability. The amplitudes are measured in units of $eL\omega_p^2/m$. The time step is $\Delta t = 5\ \omega_p^{-1}$, corresponding to $\gamma_9 \Delta t \simeq 0.05$ where $\gamma_9 \simeq 10^{-2}\omega_p$ is the growth rate of the most unstable mode $n = 9$.

The results of a simulation with $\Delta t = 5\omega_p^{-1}$ and $t_{\max} = 500\omega_p^{-1}$ are shown in Fig. 10. The excitation (or damping) rates of modes $n = 8$ to 12 from this simulation, also given in Table I, are in general agreement with the theoretical values. Note that the amplitudes of modes $n = 11$ and $n = 12$ develop a rapid oscillation for $t > 350\omega_p^{-1}$ with a period $\simeq 15\omega_p^{-1}$. This period corresponds approximately to the transit time

across a wavelength of perturbations near the boundary $v_{\min}$. These perturbations are caused by the large amplitude modes $n = 8$ and $n = 9$, and travel one wavelength $\lambda = L/11$ or $L/12$, with respect to the modes $n = 11$ or $n = 12$ in a time $\simeq 15\omega_p^{-1}$. Such oscillations may therefore be attributed to a boundary effect and may be reduced by considering a wider band of simulation particles.

II. WHISTLER WAVES

Whistler waves are circularly polarized transverse plasma waves propagating in the direction of an externally applied magnetic field $\mathbf{B}_0$. Here we assume propagation parallel to $\mathbf{B}_0$ with the wave vector potential $\mathbf{A}$ perpendicular to $\mathbf{B}_0$. Analytical studies of whistler waves [20–22] and particle simulations [23, 24] have shown the importance of resonant particle interactions in this mode, which result in collisionless damping or instability and in trapping oscillations similar to those of Langmuir waves. Electrons interacting with a whistler wave undergo changes in their velocity components $v_\parallel$ and $v_\perp$ respectively parallel and perpendicular to $\mathbf{B}_0$ and in the phase angle φ of the perpendicular velocity. In addition, we consider in the present case a nonuniform external field $\mathbf{B}_0$, having a gradient ∇B_0 in the direction of propagation, which also contributes to changes in the parallel and perpendicular velocity components. The resulting velocity increments, $\delta v_\parallel$, $\delta v_\perp$ and $\delta\varphi$ during a time step Δt, and the corresponding increment δz in the particle position parallel to $\mathbf{B}_0$ are derived in Section II.1. Test particle trajectories in a single mode field and in an external inhomogeneous field are presented in Section II.2. The equations governing the evolution of the wave vector potential are derived in Section II.3 and several examples of application are given in Section II.4.

II.1. Velocity and Position Increments

In this Section we derive an algorithm to compute the motion of electrons in electromagnetic fields represented as a sum of $n_{\max}$ cyclotron waves propagating in the z-direction along a non-uniform external magnetic field $\mathbf{B}_0(z)$. Let

$$\mathbf{A}(z, t) = \sum_{n=1}^{n_{\max}} \mathcal{A}_n(\hat{\mathbf{e}}_x \cos \psi_n + \hat{\mathbf{e}}_y \sin \psi_n), \tag{20}$$

$\mathbf{E}_w = (-1/c)\,\partial\mathbf{A}/\partial t$ and $\mathbf{B}_w = \nabla \times \mathbf{A}$ and of the external magnetic field $\mathbf{B}_\circ$ according to the momentum equation

$$\frac{d}{dt}\mathbf{v}_i = -\frac{e}{m}\left[\mathbf{E}_w + \frac{1}{c}\mathbf{v}_i \times (\mathbf{B}_w + \mathbf{B}_\circ)\right], \tag{21}$$

where $-e$ and m are the electron charge and mass, c is the velocity of light, $\mathbf{v}_i$ is the velocity of the ith electron and where the fields are evaluated at the position z_i of the electron. Employing cylindrical coordinates $(v_\parallel, v_\perp, \varphi)$ for the velocity $\mathbf{v}_i = v_{\parallel i}\hat{\mathbf{e}}_z + v_{\perp i}(\hat{\mathbf{e}}_x \cos\varphi_i + \hat{\mathbf{e}}_y \sin\varphi_i)$, Eq. (21) yields [10]

$$\begin{aligned}
\frac{d}{dt}v_{\parallel i} &= \sum_n \mathscr{U}_n k_n v_{\perp i}\sin(\varphi_i - \psi_n) - \frac{1}{2}v_{\perp i}^2\frac{1}{\Omega}\frac{d\Omega}{dz}, \\
\frac{d}{dt}v_{\perp i} &= \sum_n \mathscr{U}_n(\omega_n - k_n v_{\parallel i})\sin(\varphi_i - \psi_n) + \frac{1}{2}v_{\perp i}v_{\parallel i}\frac{1}{\Omega}\frac{d\Omega}{dz}, \\
\frac{d}{dt}\varphi_i &= \sum_n \frac{\mathscr{U}_n}{v_{\perp i}}(\omega_n - k_n v_{\parallel i})\cos(\varphi_i - \psi_n) + \Omega,
\end{aligned} \tag{22}$$

which, together with

$$\frac{d}{dt}z_i = v_{\parallel i}, \tag{23}$$

determine the dynamics of the electrons.

The fields in Eqs. (22) have been expressed through $\Omega(z) = eB_\circ/mc$, the electron gyrofrequency of the external field, and $\mathscr{U}_n(z, t) = e\mathscr{A}_n/mc$. In terms of these quantities, Eqs. (22) and (23) can be interpreted either as dimensional or as dimensionless, with time measured in units of $1/\hat{\Omega}$ and length in units of $c/\hat{\omega}_p$, $\hat{\Omega}$ and $\hat{\omega}_p$ being reference values of the gyrofrequency Ω and the plasma frequency ω_p. In this dimensionless context we assume that the inhomogeneity $\Omega^{-1}\,d\Omega/dz$ and the wave amplitude $\mathscr{U}_n$ are both of order $\epsilon \ll 1$, while all other quantities are of order unity, including $\omega_n - k_n v_{\parallel i}$ and $\Omega - \omega_n + k_n v_{\parallel i}$, which are respectively the frequency of each wave and the gyrofrequency of the electrons relative to each wave, both in the guiding center frame.

The algorithm to advance the particles during a time step Δt can be derived by integrating Eqs. (22) and (23) to order ϵ from some initial time t to $t + \Delta t$. The results can be cast in the form

$$v_{\parallel i}(t + \Delta t) = v_{\parallel i}(t) + \sum_n \delta v_{\parallel in} + \delta v_{\parallel ic}, \tag{24}$$

and similarly for $v_{\perp i}$, φ_i and z_i. Here the increments are separated into a sum of increments due to the waves $n = 1, \ldots, n_{\max}$ and a part due to cyclotron motion in

the non-uniform field denoted by the subscript c. The increments due to the wave fields are

$$\begin{aligned}
\delta v_{\parallel in} &= \mathscr{U}_n k_n v_{\perp i} \frac{\cos\zeta_{in} - \cos(\zeta_{in} + \theta_{in})}{\theta_{in}} \Delta t, \\
\delta v_{\perp in} &= \mathscr{U}_n (\omega_n - k_n v_{\parallel i}) \frac{\cos\zeta_{in} - \cos(\zeta_{in} + \theta_{in})}{\theta_{in}} \Delta t, \\
\delta\varphi_{in} &= \frac{\mathscr{U}_n}{v_{\perp i}} (\omega_n - k_n v_{\parallel i}) \frac{\sin(\zeta_{in} + \theta_{in}) - \sin\zeta_{in}}{\theta_{in}} \Delta t, \\
\delta z_{in} &= \mathscr{U}_n k_n v_{\perp i} \frac{\theta_{in}\Delta t\cos\zeta_{in} + \sin\zeta_{in} - \sin(\zeta_{in} + \theta_{in})}{\theta_{in}^2} (\Delta t)^2,
\end{aligned} \tag{25}$$

where $\zeta_{in} = \varphi_i - \psi_n$ are the phases of the electron perpendicular velocities relative to the vector potentials of the waves and $\theta_{in} = (\Omega - \omega_n + k_n v_{\parallel i})\,\Delta t$ is a resonance parameter describing to zero order the increment of the electron phase relative to the wave. The increments due to cyclotron motion are

$$\begin{aligned}
\delta v_{\parallel ic} &= -\frac{1}{2}\frac{v_{\perp i}}{v_{\parallel i}} v_{\perp i} \frac{\Omega(z_i + v_{\parallel i}\Delta t) - \Omega(z_i)}{\Omega(z_i)}, \\
\delta v_{\perp ic} &= \frac{1}{2} v_{\perp i} \frac{\Omega(z_i + v_{\parallel i}\Delta t) - \Omega(z_i)}{\Omega(z_i)}, \\
\delta\varphi_{ic} &= \tfrac{1}{2}[\Omega(z_i) + \Omega(z_i + v_{\parallel i}\Delta t)]\,\Delta t, \\
\delta z_{ic} &= [v_{\parallel i} + \tfrac{1}{2}\delta v_{\parallel ic}]\,\Delta t.
\end{aligned} \tag{26}$$

All quantities in Eqs. (25) and (26) are evaluated at the initial time t and initial position $z_i(t)$.

The limitations on the size of the time step Δt are related to errors corresponding to the omission of terms of order ϵ^2 and higher in Eqs. (25) and (26). We consider separately the errors of each equation and define the error $\bar{\delta}$ of a quantity to be the difference between the exact increment and that given by Eqs. (25) or (26).

(i) In the presence of a monochromatic wave propagating in a uniform external field, the electron energy relative to the wave coordinate system, $W_{in}^2 = [(v_{\parallel i} - \omega_n/k_n)^2 + v_{\perp i}^2]/2$, and its Hamiltonian $H_{in} = [v_{\parallel i} - (\omega_n - \Omega)/k_n]^2/2 + (\mathscr{U}_n v_{\perp i})\cos\zeta_{in}$ in the pseudopotential well of the wave must be conserved. These quantities are not conserved in the algorithm of Eq. (25) but satisfy the inequalities

$$\begin{aligned}
\frac{\bar{\delta} W_{in}^2}{W_{in}^2} &\lesssim (k_n \mathscr{U}_n \Delta t)^2, \\
\frac{\bar{\delta} H_{in}}{v_{Tin}^2} &\lesssim \frac{1}{4}(\omega_{Tin}\Delta t)^2,
\end{aligned} \tag{27}$$

where $\omega_{Tin} = k_n(\mathscr{U}_n v_{\perp i})^{1/2}$ is the trapping frequency for small oscillations of $v_{\perp i}$ relative to $-\mathbf{B}_n$ and $v_{Tin} = 2\omega_{Tin}/k_n$ is the trapping velocity. This velocity is characteristic of the velocity spread about resonance, for which the effect of the wave on the motion of the particles is large, and v_{Tin}^2 was chosen as a typical value of the Hamiltonian in the resonant region. Noting that ω_{Tin} is of order $\epsilon^{1/2}$, the most serious requirement is $(\omega_{Tin}\,\Delta t)^2 \ll 1$, imposed by the second of Eqs. (27).

(ii) In the absence of waves, the electron energy relative to the stationary frame, $V_i^2 = (v_{\parallel i}^2 + v_{\perp i}^2)/2$, and the magnetic moment $\mu_i = v_{\perp i}^2/\Omega_i$ must be conserved. The algorithm of Eq. (26) conserves energy exactly, i.e., $\delta V_i^2 = 0$, and yields a relative error in the magnetic moment given by

$$\frac{\delta\mu_i}{\mu_i} \approx \left(\frac{V_i\,\Delta t}{l_c}\right)^2, \tag{28}$$

where $l_c = \Omega(d\Omega/dz)^{-1}$ is the characteristic length of the external field inhomogeneity. In addition, the errors in the position and phase increments must be considered, since they affect the relative phase $\zeta_{in} = \varphi_i - \psi_n$. Excluding the mirror regions, where Eq. (26) is no longer valid due to the rapid variation of the parameters, these errors are given by

$$\begin{aligned} \delta z_{ic} &\approx \left(\frac{v_{\perp i}\,\Delta t}{l_c}\right)^2 v_{\parallel i}\,\Delta t, \\ \delta\varphi_{ic} &\approx 2\left(\frac{v_{\parallel i}\,\Delta t}{l_c}\right)^2 \Omega\,\Delta t. \end{aligned} \tag{29}$$

The requirements $\delta z_{ic} \ll k_n^{-1}$ and $\delta\varphi_{ic} \ll 1$ yield $(v_{\perp i}\,\Delta t/l_c)^2\, k_n v_{\parallel i}\,\Delta t \ll 1$ and $2(v_{\parallel i}\,\Delta t/l_c)^2\,\Omega\,\Delta t \ll 1$. Since in the present algorithm the time step is usually large compared to both the gyroperiod and the transit time across a wavelength, i.e., $\Omega\,\Delta t \gg 1$ and $k_n v_{\parallel i}\,\Delta t \gg 1$, Eqs. (29) give more restrictive conditions than Eq. (28).

II.2. Test Particle Trajectories

In this section we examine the accuracy of the particle-pushing algorithm, by applying it to a limited number of test electrons and comparing the numerically obtained trajectories to the theoretical results for the special cases of (i) motion in the presence of a monochromatic wave propagating in a uniform external field, and (ii) motion under the sole action of a inhomogeneous external magnetic field. This amounts to considering separately the errors in the increments given by Eqs. (25) and (26).

(i) *Motion in a Monochromatic Helical Wave*

First we consider the motion of seven test electrons in a monochromatic wave with amplitude $\mathscr{U} = e\mathscr{E}/mc = 1.88 \times 10^{-4}\Omega/k$, wavenumber $k = \omega_p/c$ and frequency

$\omega = \Omega/2$ propagating along a uniform external field specified by the electron gyrofrequency Ω. Initially all electrons have the same perpendicular velocity $v_\perp = 1.6(\Omega - \omega)/k$ (corresponding to the same trapping frequency $\omega_T = 1.23 \times 10^{-2}\Omega$ for all electrons) antiparallel to the wave vector potential, i.e., $\zeta = \varphi - \psi = \pi$. The initial parallel velocities are distributed near the resonant velocity, so that the quantity $[v_\parallel - (\Omega - \omega)/k]/v_T$, where $v_T = 2\omega_T/k$ is the trapping velocity, is respectively equal to 0, −0.5, −0.9, −1.0, −1.1, −2.5 and −6.0 for each test particle. The time step used is $\Delta t = 16/\Omega$ (corresponding to $\omega_T \Delta t = 0.197$), and the motion of each particle is followed over a total time of 100 time steps. The coordinates of the first six test electrons are plotted at every second time step in Fig. 11 in the ζ–$v_\parallel$ plane, with ζ reduced in the interval $(0, 2\pi)$ and $v_\parallel$ measured relative to $-(\Omega - \omega)/k$ in units of v_T.

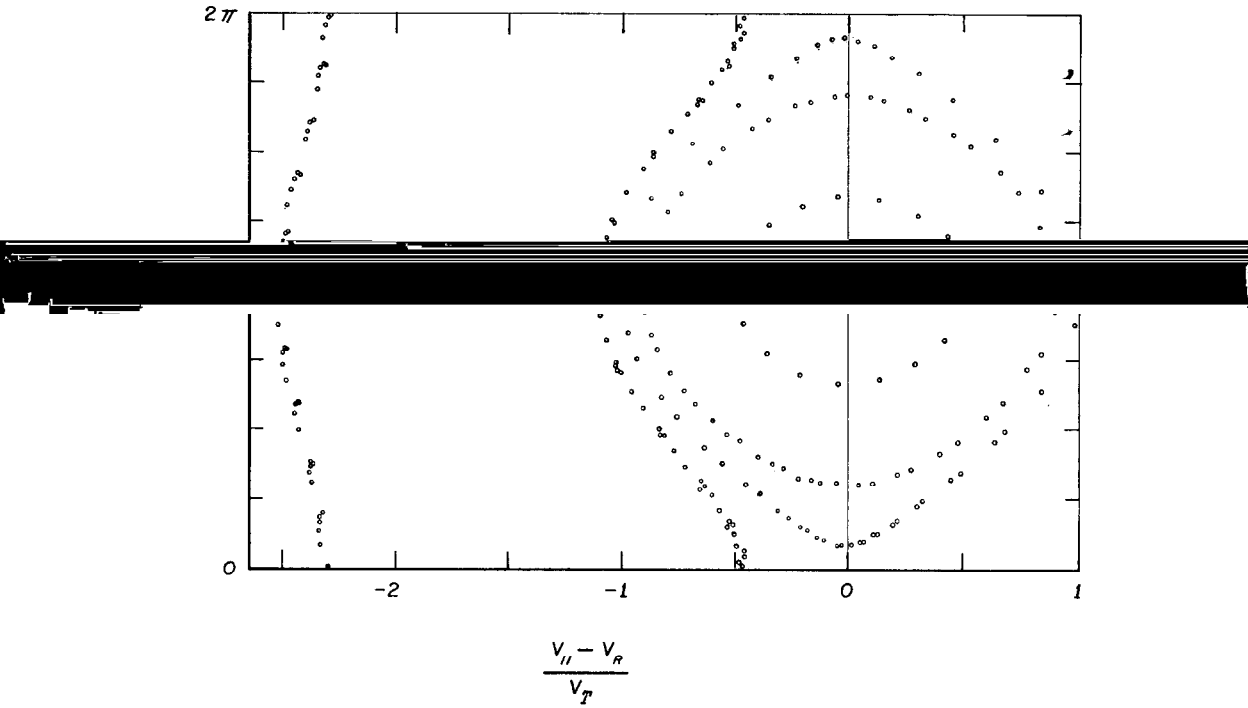

FIG. 11. Trajectories of test particles in a single-mode whistler field. Six electrons, *a*, *b*,..., *f*, with initial parallel velocities given respectively by $[v_\parallel - (\Omega - \omega)/k]/v_T = 0$, −0.5, −0.9, −1.0, −1.1 and −2.5 are shown. A time step $\Delta t = 0.197\ \omega_T^{-1}$ is used for the computation and the particle positions in the $(v_\parallel, \zeta)$ plane are shown at intervals $2\Delta t$. Note that the variable ζ is periodic with a period of 2π.

First we consider the conservation of the wave-frame kinetic energy W^2 and of the Hamiltonian H, which according to Eq. (27) are expected to incur relative errors $\delta W^2/W^2 < 9 \times 10^{-6}$ and $\delta H/v_T^2 < 10^{-2}$. The relative error in energy per time step,

averaged over the 100 time steps, is 3.5×10^{-6}, about the same for all particles, with a maximum of 8.9×10^{-6} recorded when the third electron crosses the relative phase values $\zeta = \pi/2$ and $3\pi/2$. The average relative error in the Hamiltonian is 3.7×10^{-5} for the trapped particles (a through *d*), while beyond the trapping region it increases up to 2.3×10^{-3} for the most distant untrapped particle *g* (not shown in Fig. 11). However, since the square of the trapping velocity is not a proper measure of the Hamiltonian of the untrapped particles, especially the more distant ones, it is preferable to consider the error $\delta H/H$, which, starting with an average of 1.2×10^{-4} per time step for particle *e*, decreases to 3.2×10^{-5} for the most distant particle. As expected from the singular character of the separatrix the largest relative errors in H are observed on particles *d* and *e*. This is reflected in Fig. 11 by an imperfect periodicity of the coordinates, more pronounced in particle *e*, whose velocity is shifted by $0.03v_T$ after $\omega_T t = 19.7$ (100 time steps).

A last check on the accuracy of the trajectories involves comparison of the observed periods of the trapping motion with the approximate analytical expressions, $4/\omega_T K(m)$ for trapped particles, and $2/\omega_T m^{-1/2} K(m^{-1})$ for untrapped particles. Here $K(m)$ is the complete eliptic integral of the first kind with the parameter $m = \frac{1}{2} + 2H/v_T^2$. With the exception of particle *d*, whose period cannot be calculated because of its singular behavior, the periods measured for all particles fall within 2.6% of the analytical values, which themselves are only accurate to within $v_T/v_\perp = 3.1\%$. Note that the period of particle *b* happens to be an exact multiple of twice the time step, therefore each circle for particle *b* in Fig. 11 represents its coordinates at three different times.

(ii) *Non-Uniform Cyclotron Motion*

Next we consider the motion of test electrons in an inhomogeneous external field, in absence of any wave, to evaluate the errors occurring in the increments given by Eqs. (26). To compare these errors with those of the preceding paragraph, the initial test particle velocities are chosen to correspond to the cyclotron resonance of the preceding wave ($kc/\omega_p = 1$, $\omega/\Omega = 1/2$). Thus, three electrons are initialized with parallel velocity $v_{\parallel o} = (c/2)\Omega_0/\omega_p$, equal to the resonant velocity of the reference wave and with pitch angles corresponding to a ratio $v_{\perp o}/v_{\parallel o}$ equal to 0.6, 1.0 and 1.4 respectively. These electrons are initially located at the vertex $z = 0$ of an external magnetic field giving an electron gyrofrequency $\Omega = \Omega_0(1 + z^2/l^2)$, where l is taken equal to 5300λ, $\lambda = 2\pi/k$ being the wavelength of the reference wave. This choice of the external field yields simple analytical expressions for the trajectories which can be compared to numerical results.

A time step $\Delta t = 60/\Omega_0$ is used and the motion of the electrons is followed from their initial position to each mirror point and back. The results indicate velocity errors per time step averaging 1.2×10^{-7} of their initial values, compared to 2.0×10^{-7} predicted by Eq. (28). The position and phase erorrs are constant during the first 500 time steps agreeing with the values predicted by Eqs. (29), e.g., $\delta z = 4 \times 10^{-6}\lambda$ and $\delta\varphi = 1.6 \times 10^{-5} \times 2\pi$ for the second electron. At later times, as the electrons approach the mirror points, the position and phase errors exceed the values

given by Eqs. (29), due to the finite size of Δz and to the rapid variation of the parameters, which are not accounted for in Eqs. (29).

II.3. Evolution of the Wave Vector Potential

The particle pushing algorithm of Section II.1 is used to follow the interaction of resonant electrons with whistler waves propagating parallel to the external magnetic field. The electron distribution is assumed to consist of cold electrons with density n_0 which constitute the principal propagation medium for the waves and of energetic electrons with density $n_E \ll n_0$ which are responsible for resonant interactions. It will be convenient to denote vectors perpendicular to the direction of propagation in complex form with their x components represented by the real part and their y component represented by the imaginary part as shown in Fig. 12. With this notation the vector potential corresponding to Eq. (20) takes the form

$$A(z, t) = \sum_{n=1}^{n_{\max}} \mathcal{A}_n(z, t) \exp[i\psi_n(z, t)]. \tag{30}$$

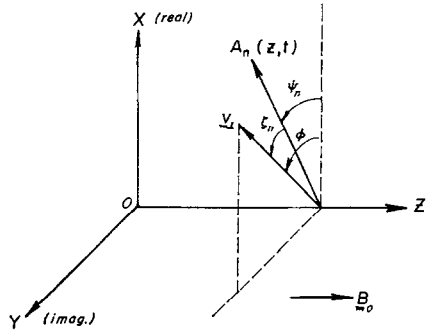

Fig. 12. Geometrical relations defining a whistler wave. $\mathbf{B}_0$ is the external magnetic field, $\mathbf{A}_n(z, t)$ is the wave vector potential of mode n and $\mathbf{v}_\perp$ is a resonant electron perpendicular velocity.

From Ampere's law, neglecting retardation effects,

$$\frac{\partial^2 A}{\partial z^2} - \frac{4\pi e n_0}{c} V = -\frac{4\pi}{c} J_E, \tag{31}$$

where V is the cold electron velocity, $-en_0V$ is the current density contribution of cold electrons and $J_E = -e \sum_i v_{\perp i} \exp(i\varphi_i)\, \delta(z - z_i)$ denotes the current density contributions of energetic electrons. Here the sum is taken over particles in a cylinder of unit cross-section perpendicular to z. The momentum equation for cold electrons yields

$$\frac{\partial V}{\partial t} - i\Omega V = \frac{e}{mc} \frac{\partial A}{\partial t}. \tag{32}$$

Integrating Eq. (32) over time yields

$$V(z,t')\exp[i\Omega(t-t')]\,|_0^t = \frac{e}{mc}A(z,t')\exp[i\Omega(t-t')]\,|_0^t + \frac{e}{mc}i\Omega\int_0^t A(z,t')\exp[i\Omega(t-t')]\,dt'.$$

Substituting Eq. (30) into this expression, expanding the integral to second order by successive integrations by parts and substituting the resulting expression into Eq. (31) gives

$$\sum_{n=1}^{n_{\max}}\left[\left(k_n^2+\frac{\omega_p^2}{c^2}\frac{\omega_n}{\omega_n-\Omega}\right)\mathscr{U}_n+\frac{\omega_p^2}{c^2}\frac{i\Omega}{(\omega_n-\Omega)^2}\frac{\partial\mathscr{U}_n}{\partial t}+2ik_n\frac{\partial\mathscr{U}_n}{\partial z}-\frac{\partial^2\mathscr{U}_n}{\partial z^2}+i\frac{\partial k_n}{\partial z}\mathscr{U}_n-\frac{\omega_p^2}{c^2}\frac{\Omega}{(\omega_n-\Omega)}\frac{\partial}{\partial t}\frac{1}{(\omega_n-\Omega)}\frac{\partial}{\partial t}\frac{\mathscr{U}_n}{\omega_n-\Omega}\right]e^{i\psi_n} = -\frac{1}{n_0}\frac{\omega_p^2}{c^2}\sum_i v_{\perp i}\exp(i\varphi_i)\,\delta(z-z_i), \tag{33}$$

where $k_n=-\partial\psi_n/\partial z$, $\omega_n=\partial\psi_n/\partial t$, $\mathscr{U}_n=e\mathscr{A}_n/mc$ and $\omega_p=(4\pi e^2n_0/m)^{1/2}$. The terms involving first order derivatives of k_n and ω_n, and the terms involving second order derivatives of $\mathscr{U}_n$ represent wavepacket dispersion in the cold plasma. For the wavepacket much longer than the wavelength considered here those terms may be neglected [24].

The wave amplitudes, wavenumbers and frequencies, $\mathscr{U}_n(z,t)$, $k_n(z,t)$ and $\omega_n(z,t)$ respectively, as well as the cyclotron frequency $\Omega(z)=eB_0/mc$, which are slowly varying functions of z are represented on a grid with mesh size Δz. For $\kappa\,\Delta z\ll 1$, where κ denotes the inverse characteristic length of the wave and of the external field B_0, these quantities may be considered constant over the interval Δz. This condition imposes an upper bound to the mesh size Δz. We now multiply Eq. (33) by $\exp(i\psi_{n'})$ and integrate over an interval Δz. For $(k_n-k_{n'})\,\Delta z\gg 1$, which implies a lower bound on the mesh size Δz, the terms $n\neq n'$ phase mix in this integration. After separating real and imaginary parts, Eq. (33) yields

$$\frac{k_n^2c^2}{\omega_p^2}-\frac{\omega_n}{\Omega-\omega_n}=-\frac{C_n}{\mathscr{U}_n} \tag{34}$$

and

$$\frac{\partial\mathscr{U}_n}{\partial t}+v_{gn}\frac{\partial\mathscr{U}_n}{\partial z}=-\frac{(\Omega-\omega_n)^2}{\Omega}S_n \tag{35}$$

where $v_{gn}=2c(k_nc/\Omega)[(\Omega-\omega_n)/\omega_p]^2$ is the group velocity of the nth wave. The source terms

$$C_n(z,t)=\frac{1}{n_0\,\Delta z}\sum_i v_{\perp i}\cos\zeta_{in}, \tag{36}$$

and

$$S_n(z, t) = \frac{1}{n_0 \Delta z} \sum_i v_{\perp i} \sin \zeta_{in}, \tag{37}$$

where $\zeta_{in} = \varphi_i - \psi_n(z_i, t)$, account for the effect of energetic particles on the propagation of each wavepacket. The sums in Eqs. (36) and (37) extend to particles located within a cylinder of unit cross-section perpendicular to z and in the interval $(z - \Delta z/2, z + \Delta z/2)$ along z. We note that the upper and lower bounds imposed on the mesh size Δz imply $\kappa \ll k_n - k_{n'}$ for any $n \neq n'$, i.e., the wavelength of the beat oscillation of two waves must be short compared to the scale length of the inhomogeneities. Differentiating Eq. (34) with respect to time yields the equation of propagation of the frequency of wave n,

$$\frac{\partial \omega_n}{\partial t} + v_{gn} \frac{\partial \omega_n}{\partial z} = \frac{(\Omega - \omega_n)^2}{\Omega} \frac{\partial}{\partial t} (C_n / \mathscr{U}_n). \tag{38}$$

The source terms C_n and S_n depend on the correlation of the phase of the electrons perpendicular velocities with respect to the phase of the wave vector potential. These terms account for cyclotron damping or excitation of the waves or for secondary emissions caused by resonant energetic particles. Numerical simulations of these effects may therefore be carried out by following the wave propagation in terms of Eqs. (34), (35) and (38) while advancing energetic resonant electrons with the algorithm of Section II.1, the source terms C_n and S_n being updated after each time step. Here a band of simulation particles covering the resonant region of the waves is usually sufficient. The initial loading of simulation particles within the resonance region may be done either randomly or in ordered manner. The examples presented in Section II.4 were carried out with particles having a random initial distribution monoenergetic in the perpendicular direction. Initially, each particle is given a random parallel velocity, $v_\parallel$, with a distribution simulating the desired initial electron distribution in the resonance region. All particles are given the same perpendicular velocity, $v_\perp$, but their phase angles, φ, are chosen with a random uniform distribution in the interval $(0, 2\pi)$. Quiet start methods in which the particles are initialized in an ordered manner must be delayed by staggering the particles initial parallel velocities and the physical effects being studied must occur in a time shorter than the growth time of the beaming instability [9].

II.4. Examples of Long-Time-Scale Simulations

In this section we present applications of the algorithm to the classical cases of (i) the cyclotron two-beam instability and (ii) the cyclotron damping of a large-amplitude whistler wave. In these computations the resonant energetic electrons are advanced at each time step according to Eq. (24) and the wave amplitude and frequency is

propagated according to Eqs. (34) to (38). In both cases periodic boundary conditions are imposed and the length of the system is taken equal to the wavelength $\lambda = 2\pi/k$ of the wave.

(i) *Cyclotron Two-Beam Instability*

This instability occurs with an initial distribution of the electrons given by

$$f(\mathbf{v}, t = 0) = (1 - \epsilon_b)\frac{1}{v_\perp}\delta(v_\parallel)\,\delta(v_\perp) + \epsilon_b \frac{1}{v_\perp}\delta(v_\parallel - v_{\parallel b})\,\delta(v_\perp - v_{\perp b}), \quad (39)$$

where the first term corresponds to the cold plasma with density $1 - \epsilon_b$, and the second term represents a beam with density $\epsilon_b \ll 1$ and initial velocities $v_{\parallel b}$, $v_{\perp b}$ respectively parallel and prependicular to the external magnetic field $\mathbf{B}_0$. In the present case the dispersion relation for the whistler mode [20],

$$\left(\frac{kc}{\omega_p}\right)^2 = \left(\frac{\omega}{\omega_p}\right)^2 - \int d\mathbf{v}\left[\frac{kv_\parallel - \omega}{kv_\parallel - \omega + \Omega} + \frac{1}{2}\left(\frac{kv_\perp}{kv_\parallel - \omega + \Omega}\right)^2\right] f(\mathbf{v}), \quad (40)$$

yields for $(\omega/k) \ll c$ (i.e., neglecting displacement current),

$$x^3 + \left(kv_{\parallel b} + \frac{\Omega}{d}\right)x^2 + \frac{\epsilon_b}{d}\left(\Omega k v_{\parallel b} + \frac{1}{2}k^2 v_{\perp b}^2\right)x + \frac{\epsilon_b}{2d}k^3 v_{\parallel b} v_{\perp b}^2 = 0, \quad (41)$$

where $d = 1 + (kc/\omega_p)^2$. The real part of x determines the frequency shift $\tilde{\omega} = \omega - (\Omega + kv_{\parallel b}) = \mathrm{Re}(x)$, and its imaginary part determines the growth rate, $\gamma = \mathrm{Im}(x)$ of the wave. For $kc/\omega p = 1$ and $kv_{\perp b} = \Omega$, the maximum growth rate, $\gamma = (\sqrt{3}/4)(\epsilon_b)^{1/3}\,\Omega$, occurs at $kv_{\parallel b} = -\Omega/2$ and corresponds to a frequency shift $\tilde{\omega} = -(1/4)(\epsilon_b)^{1/3}\,\Omega$.

The results of a computer simulation corresponding to these parameters for a beam with relative density $\epsilon_b = 10^{-6}$ represented by 600 simulation particles are given in Fig. 13. The wave, initially set up with amplitude $eB/mc = 10^{-7}\Omega$, grows exponentially with a rate $\gamma = 4.3 \times 10^{-3}$ to a saturation value $eB_s/mc \approx 6 \times 10^{-4}\Omega$ corresponding to a trapping frequency $\omega_{Ts} = 6.5 \times 10^{-3}\Omega$. The time step used is equal to $\Delta t = 6.3\Omega^{-1}$, corresponding to $\omega_{Ts}\,\Delta t = 0.041$ and $\gamma\,\Delta t = 0.027$. We note in Fig. 13a that, except for an initial period of adjustment between the energetic electrons and the wave, the exponential growth of the wave agrees closely with the theoretical growth rate, indicated in Fig. 13a by a straight broken line. The frequency shift, plotted in Fig. 13b, approaches the theoretical frequency $\tilde{\omega}_{th} = -2.5 \times 10^{-3}\Omega$, indicated by a horizontal broken line. After saturation the amplitude and the frequency undergo oscillations with period given by the trapping frequency at saturation. These oscillations are practically undamped, since the initially monoenergetic beam requires many trapping periods in order to be significantly phase-mixed.

It is recalled from Eq. (27) that the particle pushing algorithm does not conserve energy exactly. For the case considered here, the total energy is $W_t = W_w +$

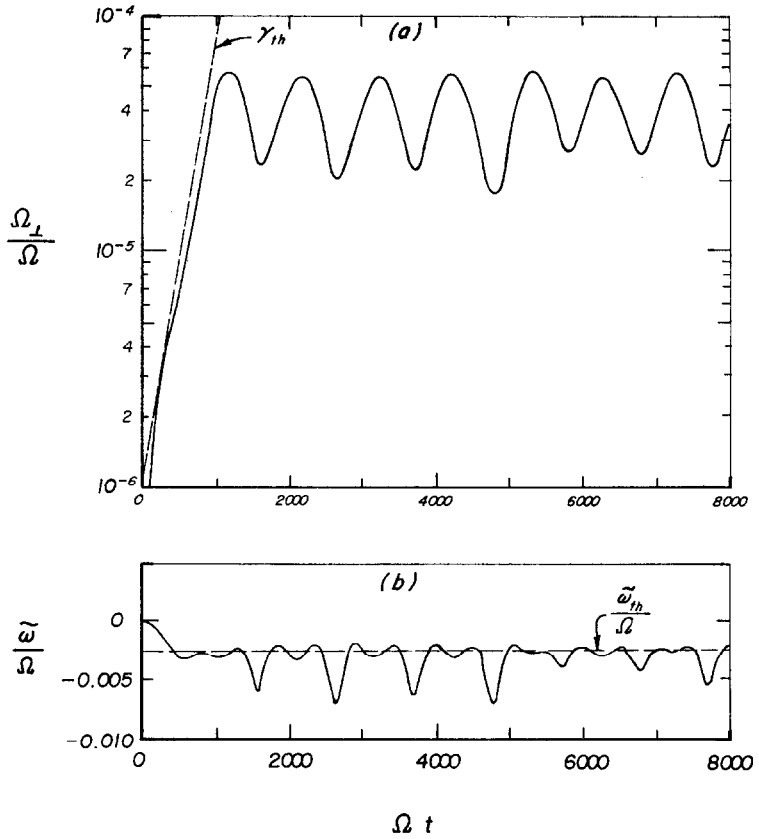

FIG. 13. Wave amplitudes and frequency shift for the whistler instability and trapping of a monoenergetic beam. The amplitude is measured in terms of the ratio $\Omega_\perp/\Omega = B/B_0$ where B is the wave magnetic field amplitude and B_0 is the external magnetic field. A time step $\Delta t = 6.3\ \Omega^{-1}$ was used.

$W_\parallel + W_\perp$, where $W_w = mn_p\omega\Omega\mathscr{U}^2/2(\Omega - \omega)^2$ accounts for the energy of the wave, $W_\parallel = mn_p\epsilon_b\langle v_\parallel{}^2\rangle/2$ is the kinetic energy of the beam in the parallel direction and $W_\perp = mn_p\epsilon_b\langle v_\perp{}^2\rangle/2$ is its energy in the perpendicular direction. The variations in W_w, $W_\parallel$, $W_\perp$ and W_t are separately plotted in Fig. 14. Note that the variation in the total energy W_t, which is plotted on an expanded scale increases at a rate $2 \times 10^{-10}\frac{1}{2}mn_p(c\Omega/\omega_p)^2$ per trapping period. This rate depends on the magnitude of the time step. Simulations with larger time steps, up to $\Omega\ \Delta t = 100$, give a numerical increase of the amplitude after saturation, while the initially linear growth of the wave still follows accurately the theoretical prediction.

(ii) *Cyclotron Damping of a Large-Amplitude Whistler Wave*

The transfer of energy between a large-amplitude monochromatic whistler wave and resonant energetic electrons has been studied theoretically [21, 22] and by

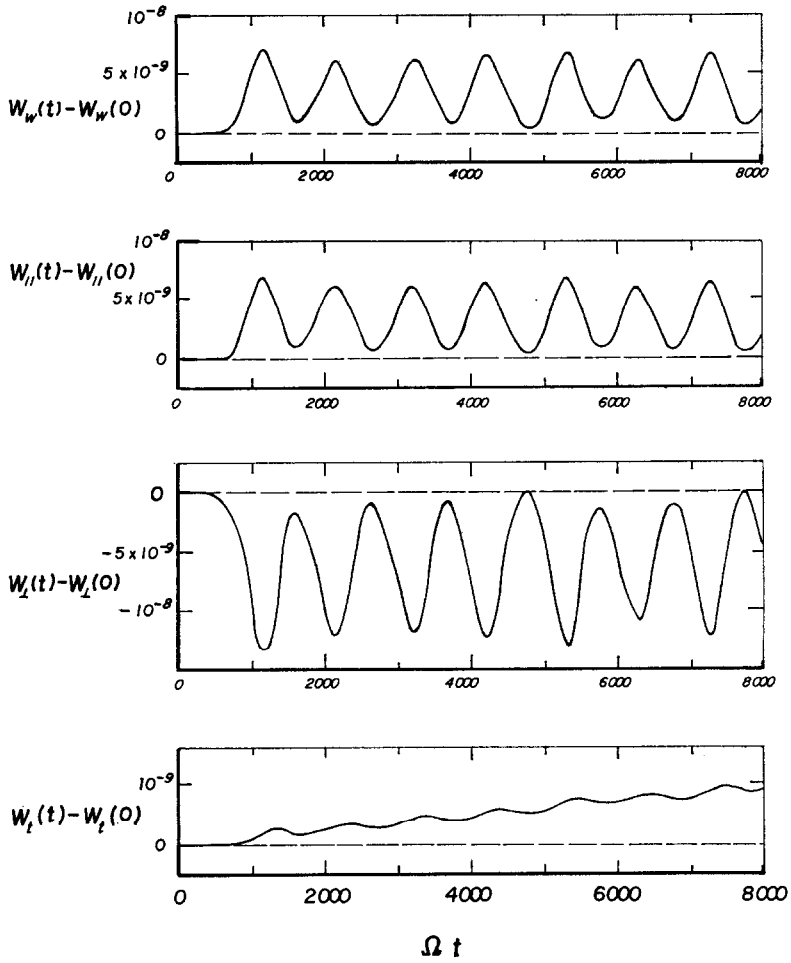

FIG. 14. (a) Wave energy density, $W_w = mn_p\omega\Omega\mathcal{U}^2/2(\Omega - \omega)^2$; (b) beam kinetic energy density in parallel direction, $W_\parallel = mn_p\epsilon_b \langle v_\parallel{}^2\rangle/2$; (c) beam kinetic energy density in perpendicular direction, $W_\perp = mn_p\epsilon_b\langle v_\perp{}^2\rangle/2$; (d) total energy density, $W_t = W_w + W_\parallel + W_\perp$. Units are $mn_p(c\Omega/\omega_p)^2/2$. Note that W_t is plotted on an expanded scale.

computer simulations [11, 23]. For times, $t \lesssim \omega_T^{-1}$, shorter than the inverse trapping frequency, $\omega_T = (kv_\perp\Omega_\perp)^{1/2}$ where $\Omega_\perp = eB/mc$, the wave amplitude B decreases at the cyclotron damping rate γ_L. Solution of the dispersion relation, Eq. (40), for a resonant velocity $v_R = (\omega - \Omega)/k$ much larger than the thermal velocity yields

$$\gamma_L = \frac{\pi^2\omega_p{}^2\omega}{k^2c^2}\left(\frac{\omega}{\Omega} - 1\right)\int_0^\infty v_\perp{}^3\, dv_\perp \left(\frac{\partial f}{\partial v_\parallel} + \frac{\Omega}{kv_\perp}\frac{\partial f}{\partial v_\perp}\right)_{v_\parallel = v_R}. \tag{42}$$

This damping rate may also be derived from energy considerations [25]. After integration with respect to $v_\perp$ Eq. (42) yields

$$\gamma_L = \pi^2 \frac{(\Omega - \omega)^2}{\Omega} \left[2 \frac{\Omega}{k} \eta_1(v_R) - \left(\frac{d\eta_2}{dv_\parallel} \right)_{v_\parallel = v_R} \right] \tag{43}$$

where $\eta_1(v_\parallel) = \int_0^\infty v_\perp f \, dv_\perp$ and $\eta_2(v_\parallel) = \int_0^\infty v_\perp^3 f \, dv_\perp$. For times $t \gtrsim \omega_T^{-1}$, the wave amplitude is modulated at approximately the trapping frequency ω_T in a manner similar to the case of a large-amplitude Langmuir wave.

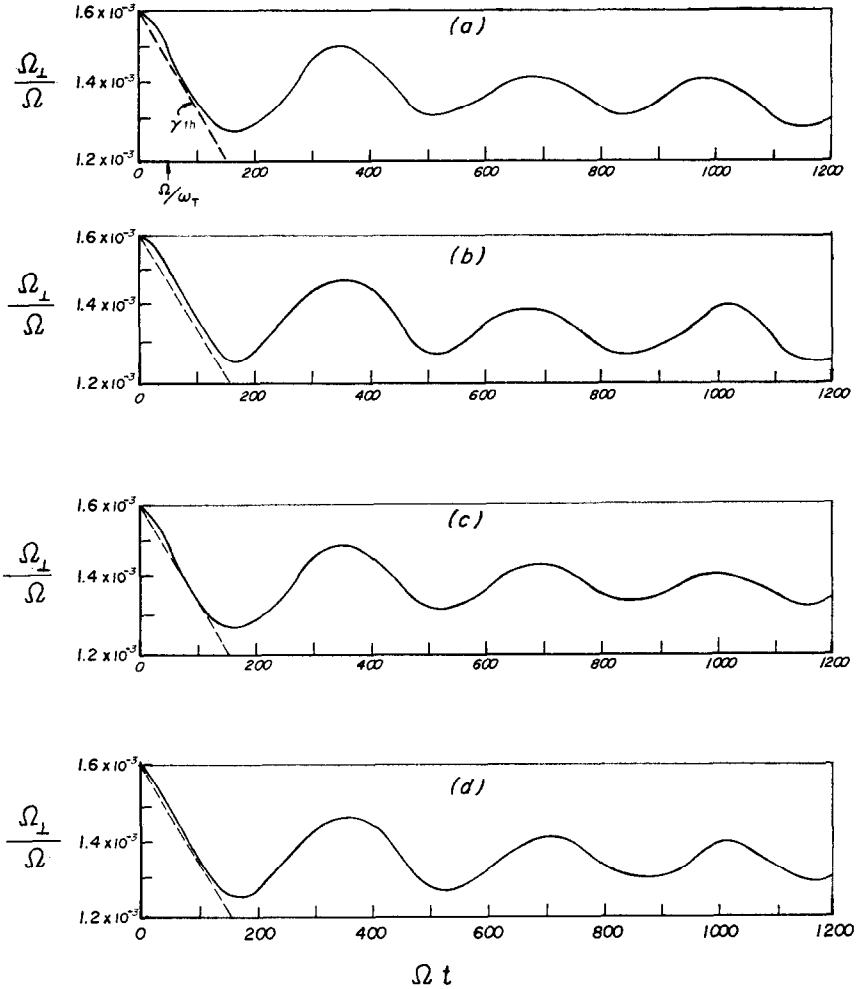

FIG. 15. Wave amplitude for a large-amplitude whistler wave. (a) $\Delta t = 10\ \Omega^{-1}(\omega_T \Delta t = 0.2)$ with a cut-off velocity $v_c = 1.5\ v_T$; (b) $\Delta t = 10\ \Omega^{-1}(\omega_T \Delta t = 0.2)$ with a cut-off velocity $v_c = 3.1\ v_T$; (c) $\Delta t = 5\ \Omega^{-1}(\omega_T \Delta t = 0.1)$ with a cut-off velocity $v_c = 1.5\ v_T$; (d) $\Delta t = 5\ \Omega^{-1}(\omega_T \Delta t = 0.1)$ with a cut-off velocity $v_c = 3.1\ v_T$. The broken straight lines indicate the initial theoretical linear damping rate.

In the present simulation of this phenomenon we consider an energetic electron distribution function which is monoenergetic in the perpendicular direction and uniform in the parallel direction in the region near the resonant velocity, $f_E = \epsilon\delta(v_\perp - v_{\perp 0})/2\pi v_{\perp 0}^2$ where $\epsilon = n_E/n_0$. In this case $(d\eta_2/dv_\parallel)_{v_\parallel = v_R} = 0$ and with $\omega = \Omega/2$, $kc/\omega_p = 1$, $v_{\perp 0} = 0.25c\Omega/\omega_p$ and $\epsilon = 0.625 \times 10^{-3}$, the first term in bracket in Eq. (43) yields a cyclotron damping rate $\gamma_L = 1.96 \times 10^{-3}\Omega$. The initial amplitude, corresponding to $\Omega_\perp/\Omega = 1.6 \times 10^{-3}$ gives an initial trapping frequency $\omega_T = 2 \times 10^{-2}\Omega$. The simulation particles are initialized with uniformly distributed random position, phase angles and parallel velocities. The parallel velocities are limited to an interval $v_R - v_c < v_\parallel < v_R + v_c$ of half width v_c.

The results of several computations with 1000 simulation particles per trapping velocity v_T are given in Fig. 15. The field amplitude, plotted on a logarithmic scale at (a) was obtained with a time step $\Delta t = 0.2\omega_T^{-1}$ and a half width $v_c = 1.5v_T$. It is observed to decay for $t \lesssim 100\Omega^{-1}$ at a rate close to the theoretical value $\gamma_L = 1.96 \times 10^{-3}\Omega$ shown as a broken line, and for longer times the expected amplitude modulation occurs with a period equal to the trapping period $\tau_{Tav} = 344\Omega^{-1}$ corresponding to the mean amplitude ratio $\langle\Omega_\perp\rangle/\Omega = 1.4 \times 10^{-3}$. For $t \gg \tau_T$ the amplitude of the modulation decays due to phase mixing of the trapped electrons. The results of additional computations with $\Delta t = 0.2\omega_T^{-1}$, $v_c = 3.1v_T$, $\Delta t = 0.1\omega_T^{-1}$, $v_c = 1.5v_T$ and $\Delta t = 0.1\omega_T^{-1}$, $v_c = 3.1\ v_T$ are given respectively in Figs. 15b,c and d. In the present computations, boundary effects which would result from density discontinuities at $\pm v_c$ are avoided by allowing the density of simulation particles to fall linearly to zero in two boundary regions of width $0.5v_c$ located outside the primary simulation region $v_R - v_c < v_\parallel < v_R + v_c$.

Conclusions

We have presented in this paper numerical algorithms to compute the motions of charged particles in Langmuir and in whistler waves, in which the particles are advanced during each time step according to their first-order motions with respect to the wave fields. The non-linear dynamics of the particles is obtained as a result of the repeated updatings of the positions and velocities after each time step. This algorithm is applicable to numerical simulations of resonant interactions of low density energetic electrons with waves propagating in a dense, low-energy plasma, on a long time scale compared to the electron plasma period, $2\pi/\omega_p$, the electron cyclotron period, $2\pi/\Omega$, or the electron transit time across a wavelength, $(kv)^{-1}$. The time step Δt is limited by the trapping periods of electrons in the waves, $\Delta t \ll \omega_T^{-1}$, and by the spatial and temporal rates of change of the wave spectrum $\Delta t \ll (\kappa v)^{-1}$ and $\Delta t \ll T$, where κ and T are respectively the inverse scale length and the characteristic time of the wave amplitudes, frequencies and wave numbers.

The present algorithm may be applied either to particle simulations or to numerical solutions of the Vlasov equation. In particle simulations, the evolution of a given set of simulation particles is followed in time through the entire duration of the compu-

tation, while in Vlasov solutions, values of the distribution function are advanced only a single time step in phase space, after which the distribution function is reconstructed on a grid. In the case of Langmuir waves, which corresponds to a two-dimensional phase space (x, v_x), a Vlasov solution of the energetic electrons distribution function was presented in Part I. However, particle simulations are also possible. In the whistler case presented in Part II, only particle simulations appear practicable since the representation of phase space regions on a four-dimensional grid (z, v_x, v_y, v_z) would require a number of points which exceeds present computer capabilities.

The fields in the present algorithm are specified in terms of their spectral representation, rather than on a spatial grid, and the position and velocity increments of the particles must be computed for each mode. This results in a computing time proportional to the product $Nn_{\max}$ of the number of particles, N, by the number of modes, $n_{\max}$, and implies a limitation of the method in the case of broad bandwidth problems requiring a large number of modes. We note that the trigonometric functions in Eqs. (9), (10), and (25) are smooth and may be evaluated by a combination of table look-up and interpolation, with a computing time requirement comparable to the electric field evaluation of conventional particle simulation methods.

In the case of Vlasov solutions, applicable to Langmuir waves, an efficient computation procedure based on fast Fourier transforms is possible. Since particles, in this case, always start from positions and velocities at the grid points, $x_j = j\,\Delta x$ and v_k, Eqs. (9) and (10) may be written in the form

$$\delta v_{jk} = \mathrm{Re} \sum_{n=1}^{J} A_{kn} \exp(2\pi nj/J), \tag{44}$$

$$\delta x_{jk} = v_k\,\Delta t + \mathrm{Re} \sum_{n=1}^{J} B_{kn} \exp(2\pi nj/J), \tag{45}$$

where the number of modes is taken equal to the number of spatial grid points $(J = n_{\max})$, and

$$A_{kn} = \frac{e}{m}\,\mathscr{E}_n\,\Delta t\,\frac{\exp(i\theta_{kn}) - 1}{\theta_{kn}} \exp(i\alpha_n),$$

$$B_{kn} = -\frac{e}{m}\,\mathscr{E}_n\,\Delta t^2\,\frac{\theta_{kn} + i[\exp(i\theta_{kn}) - 1]}{\theta_{kn}^2} \exp(i\alpha_n).$$

Thus the velocity and position increments can be computed through Eqs. (44) and (45) by taking Fourier transforms of the coefficients A_{kn} and B_{kn} for each velocity v_k. This results in a computation time proportional to $N \log_2 n_{\max}$ where N is the number of phase points.

The computation of position and velocity increments δx_{in} (or δz_{in}) and δv_{in} (or $\delta \mathbf{v}_{in}$), as well as the computation of the source terms C_n and S_n, in Langmuir (or whistler) waves, depends on the phases ψ_{in} (or ζ_{in}) of the particles relative to the waves. The

particle position x_i (or z_i) enters directly in the computation only through the slowly varying amplitudes, $\mathscr{E}_n$ (or $\mathscr{U}_n$), frequencies, ω_n and Ω, and wave numbers, k_n. Therefore, in particle simulations, the spatial distribution of particles does not need to be dense with respect to each wavelength, but needs to be dense only with respect to the scale length of the wave amplitudes, frequencies and wave numbers. The possibility of using a sparse spatial distribution of particles, and to consider only the resonant regions of phase space allows simulations in long systems which would not be possible with conventional particle simulation methods. We should note, however, that a sparse spatial distribution of phase points in Vlasov solutions is not possible, since the phase of a particle with respect to a wave is not preserved after reconstruction of the distribution function, unless the condition $k\,\Delta x \ll 1$ is satisfied.

ACKNOWLEDGMENTS

This work is supported jointly by the Office of Naval Research under contract N00014-75-0473 and by the U.S. Energy Research and Development Administration under contract EY-76-S-02.2200. Acknowledgment is made to the National Magnetic Fusion Energy Computing Center and to the National Center for Atmospheric Research, which is sponsored by the National Science Foundation for computer time used in this research. This research was done in cooperation with R. N. Sudan, whose work is supported by the Atmospheric Sciences division of the National Science Foundation under grant ATM75-02797A01.

REFERENCES

1. J. M. DAWSON AND R. SHANNY, *Phys. Fluids* **11** (1968), 1506.
2. R. L. MORSE AND C. W. NIELSON, *Phys. Fluids* **12** (1969), 2418.
3. C. K. BIRDSALL AND D. FUSS, *J. Computational Phys.* **3** (1969), 494.
4. A. BRUCE LANGDON, *J. Computational Phys.* **6** (1970), 247.
5. W. L. KRUER, J. M. DAWSON, AND B. ROSEN, *J. Computational Phys.* **13** (1973), 114.
6. J. DENAVIT, *J. Computational Phys.* **9** (1972), 75.
7. C. E. RATHMANN AND J. DENAVIT, *J. Computational Phys.* **18** (1975), 165.
8. I. HABER, C. E. WAGNER, J. P. BORIS, AND J. M. DAWSON, "Proceedings of the Fourth Conference on Numerical Simulation of Plasmas," p. 126, Naval Research Laboratory, Washington, D.C., 1970.
9. J. DENAVIT, *J. Computational Phys.* **15** (1974), 449.
10. R. N. SUDAN AND E. OTT, *J. Geophys. Res.* **76** (1971), 4463.
11. R. N. SUDAN AND J. DENAVIT, *Phys. Today* **26**, No. 12 (1973), 32.
12. C. E. RATHMANN, Ph.D. Dissertation, Northwestern University, 1975.
13. C. E. RATHMANN AND J. DENAVIT, "Proceedings of the 7th Conference on Numerical Simulation of Plasmas," New York University, June 1975.
14. This algorithm is similar but not identical to Filon's quadrature formula, (comment by A. B. Langdon) see L. N. G. FILON, *Proc. Roy. Soc. Edinburgh A* **49** (1928), 38; also Z. KOPAL, "Numerical Analysis," pp. 408–410, Chapman & Hall, London 1955. A similar method is also used in a different context to determine electron trajectories in vacuum diode regions in the presence of time varying gap fields, see C. K. BIRDSALL AND W. B. BRIDGES "Electron Dynamics of Diode Regions," Academic Press, New York, 1966.
15. T. O'NEIL, *Phys. Fluids* **8** (1965), 2255.

16. V. L. Bailey, Jr. and J. Denavit, *Phys. Fluids* **13** (1970), 451.
17. Y. Matsuda and F. W. Crawford, *Phys. Fluids* **18** (1975), 1336, 1346.
18. V. E. Zakharov and V. I. Karpman, *Zh. Eksp. Teor. Fiz.* **43** (1962), 490 [*Sov. Phys. JETP* **16** (1963), 351].
19. J. Denavit, B. W. Doyle, and R. H. Hirsch, *Phys. Fluids* **11** (1968), 2241.
20. R. N. Sudan, *Phys. Fluids* **6** (1963), 57 (Eq. 9d); see also T. F. Bell and O. Buneman, *Phys. Rev.* **133** (1964), A1300.
21. R. F. Lutomirski and R. N. Sudan, *Phys. Rev.* **147** (1966), 156.
22. P. Palmadesso and G. Schmidt, *Phys. Fluids* **14** (1971), 1411.
23. S. L. Ossakow, I. Haber, and R. N. Sudan, *Phys. Fluids* **15** (1972), 935.
24. J. Denavit and R. N. Sudan, *Phys. Fluids* **18** (1975), 1533.
25. N. I. Bud'ko, V. I. Karpman, and O. A. Pokhotelov, *Cosmic Electrodynamics* **3** (1972), 147.